Optical Materials 167 (2025) 117294

Contents lists available at ScienceDirect

Optical Materials

journal homepage: www.elsevier.com/locate/optmat

Mid-infrared optical fiber Devices: Challenges, advances and applications

Francesco Anelli, Antonella Maria Loconsole, Francesco Prudenzano *

Department of Electrical and Information Engineering, Polytechnic University of Bari, 70125, Bari, Italy

A B S T R A C T

This review provides an overview on part of the several recent progresses in mid-infrared optical fiber devices, with a focus on enabling technologies and emerging applications. The mid-infrared spectral region is of particular interest due to its strong and selective molecular absorption, which is a key element for high-sensitivity applications such as gas sensing, chemical and biomedical sensing, and environmental monitoring. The paper first outlines the significance of the mid-infrared wavelength window and its application landscape. Then, it reports the state-of-the-art of mid-infrared optical sources, including those based on nonlinear frequency conversion and fiber laser architectures. Special emphasis is then placed on recent developments in fiber-based components that support the fabrication of compact, mechanically robust, and alignment-free, all-fiber mid-infrared systems. In particular, fluoride glass fibers, owing to their broad transmission wavelength range and low phonon energy, have emerged as a practical platform in this area. The review highlights the substantial research efforts devoted to improving the performance, fabrication, and integration of fluoride fiber technologies, which are expected to play a crucial role in the advancement of next-generation mid-infrared photonic systems.

1. Introduction

The exploitation of mid-infrared (Mid-IR) electromagnetic spectral range, which includes wavelengths from $\lambda = 2.0\ \mu m$ to $\lambda = 20\ \mu m$, is nowadays definitely considered an enabling strategy towards novel and intriguing scientific breakthroughs and, consequently, towards technologically advanced applications [1–3]. Among the application areas, there are medicine, with laser surgery and diagnostic imaging; chemical detection; on-site environmental monitoring; remote sensing; industrial applications as material processing and material science; metrology; innovative guided optics and free propagation communications. For these reasons, the Mid-IR optical systems are becoming increasingly attractive, promising feasible tools to be exploited not only in fundamental research but also for practical applications, allowing the improvement of the quality of everyday life. The disruptive impact related to the exploitation of this wavelength range is due to several occurrences/factors which can be included in two main categories.

i) The first factor is the peculiarity of Mid-IR light-matter interaction, which is characterized by absorption peaks allowing the identification of unique fingerprints. This is experimented in a plethora of materials when irradiated at Mid-IR wavelengths and originated by the chemical properties of the involved substances. Molecules to be detected in monitoring systems and more specifically biomolecules, e.g. proteins, carbohydrates, nucleic acids, and lipids are characterized by very complex chemical bonds. Due to their complexity, they uniquely interact with Mid-IR light. The most important mechanism is photon absorption, causing molecular vibrations, rotations, rotational-vibration transitions. These phenomena are related to different mechanisms within the molecules such as stretching, bending and rotational motions. Therefore, for several molecules, characteristic absorption spectra can be detected, allowing qualitative and quantitative monitoring [4].

Any Mid-IR monitoring system needs an optical source, better if tunable in wavelength. Among the sources, there are the quantum cascaded lasers (QCLs), the inter-band cascade lasers (ICLs), the Mid-IR Light Emitting Diodes (LEDs), the external cavity coupled QCL (ECQCL), the vertical external-cavity surface-emitting laser (ECSEL), the rare earth (RE) doped fiber laser, and the broadband sources based on non-linear (NL) phenomena as the super continuum generation (SCG) or the shifting toward longer wavelengths as occurs in the soliton shifting fiber systems. In the following, rare earth doped fiber lasers will be considered more in depth.

The optical sources are employed to generate a range of wavelengths, interacting with the material samples as contaminated solid, liquid or gas mixtures or biomaterials. As well known, other fundamental parts of the monitoring systems are the transducers. They are suitable interfaces where the chemical/biological samples or biological matrices such as urine, saliva, blood tissues, interact with Mid-IR light, thus obtaining molecular-finger prints. Finally, the

This article is part of a special issue entitled: 80th birthday of Giancarlo C. Righini published in Optical Materials.

* Corresponding author.

E-mail address: francesco.prudenzano@poliba.it (F. Prudenzano).

https://doi.org/10.1016/j.optmat.2025.117294

Received 30 May 2025; Received in revised form 1 July 2025; Accepted 1 July 2025

Available online 3 July 2025

detecting stage is devoted to recording the intensity/characteristic of the Mid-IR beam after the light-matter interaction with the sample. It is followed by a processing unit for signal investigation. Among the kinds of detectors, there are the indium antimonide (InSb), the mercury cadmium telluride semiconductor (MCT), the deuterated triglycine sulfate (DTGS), the quantum cascade (QCD), the pyroelectric and the thermopile ones [4]. It is schematically illustrated in Fig. 1.

ii) The second factor is related to the advances on Mid-IR technologies, including also the development of glass materials, successfully employed for the construction of passive devices such as optical combiners, power dividers, optical gratings, photonic lanterns, optical sensors, offering a new platform towards the construction of all in fiber devices; to the recent development of high-performance continuous wave, pulsed and super continuum optical sources; to the cost lowering of the available on market Mid-IR bulk devices, to be employed in the measurement set-ups.

Providing an exhaustive panorama on Mid-IR advances is very hard, due to the large literature production. This review reports only a selection of recent state-of-the-art developments but gives an idea on the level of interest and potential impact of the topic. It is organized with the following sections: Sect. 2. Mid-IR Light-matter interaction; Sect. 3. Mid-IR Imaging; Sect. 4. Recent advances in Mid-IR optical fibers/materials; Sect. 5. Mid-IR Optical sources; Sect. 6. Key elements for integrated Mid-IR all in fiber systems; Sect. 7. Conclusion.

2. Mid-IR light-matter interaction

With reference to the Mid-IR light-matter interaction, a number of solids, liquids and gases are made of molecules exhibiting peculiar absorption peaks in the Mid-IR wavelength region. The recovering of their fingerprints enables innovative Mid-IR sensing set-ups which promise high social impact.

As an example, atmospheric polluting gases such as nitrogen oxides NO_x, sulfur dioxide SO_2, ammonia NH_3, and black carbon BC are present within urban areas, around landfills and seaports. Their detection is strongly required to reduce human diseases causing high social costs. Nitrogen oxides are characterized by Mid-IR absorption peaks typically around $\lambda = 5.26\ \mu m$ for nitrogen monoxide NO [5], $\lambda = 3.4\ \mu m$, $\lambda = 6.2\ \mu m$, $\lambda = 13.3\ \mu m$ for nitrogen dioxide NO_2 [6,7]. Sulfur dioxide SO_2 exhibits typical absorption bands, overall around $\lambda = 4.0\ \mu m$, $\lambda = 7.4\ \mu m$, and $\lambda = 8.6\ \mu m$ [8–10]. Ammonia NH_3 has multiple absorption spectra around $\lambda = 2.2 - 2.3\ \mu m$ and $\lambda = 9.0 - 10.6\ \mu m$ [11,12]. Furthermore, other atmospheric molecules such as carbon dioxide CO_2 and carbon monoxide CO exhibit characteristic absorption peaks at the wavelengths $\lambda = 4.26\ \mu m$ and $\lambda = 4.65\ \mu m$, respectively [13,14].

With reference to biomedicine, lipids and proteins are associated with absorptions bands between $\lambda = 2.6\ \mu m$ and $\lambda = 3.8\ \mu m$, at different wavelengths. Particular spectral fingerprints are ascribed, in the $\lambda = 2.8 - 3.2\ \mu m$ wavelength band, to protein and water absorption and, in the $\lambda = 3.2 - 3.6\ \mu m$ wavelength band, to fatty acids and cholesterol esters [1].

Differential damage technique based on differential absorption of different tissues was applied in Ref. [1]. With this technique, biological tissues can be heated to a temperature lethal to cells by laser radiation in the absorption band. The samples can be prepared by a specialized precision cutting instrument, e.g. via microtome technique, to have a uniform thickness. The adipose tissue exhibits stronger absorption peaks associated with the fatty acids in the $\lambda = 3.2 - 3.6\ \mu m$ wavelength band if compared with artery and muscle tissues [1].

Mid-IR imaging is another promising field. In the transmission mode, micro-spectroscopic imaging has been demonstrated to be feasible in different cases. Lasers with low power can overcome the large absorption loss and allow reflectance imaging to a depth of several 10's or 100's of μm of thin biotissue layers as blood and lipid ones. The high brightness/low noise characteristics of optical fiber lasers can lead to real-time or almost real-time imaging also for Mid-IR in-vivo diagnostics [15].

Moreover, Mid-IR breath analysis has attracted relevant attention within the medical community. It has emerged as an efficient approach for biomedicine diagnostics, thanks to its noninvasive implementation and its real-time monitoring potential [16–19]. Indeed, human breath, being a complex mixture of gases such as water vapor, oxygen, carbon dioxide, nitrogen, and hosting low quantity or traces of about a thousand molecules, can offer very important information about human health and can allow scientific investigation into the coming diseases and their related risks. Indeed, these molecules are generated internally by the human body or absorbed from contact with the external environment. Their presence and overall knowledge of their concentration constitutes a fertile ground for medical diagnostics.

The exploitation of Mid-IR lasers in high-precision surgery is particularly interesting by generating radiation in the protein absorption $\lambda = 6 - 8\ \mu m$ wavelength band, this allowing a strongly reduced traumatic approach. The radiation from a pulsed-periodic, Holmium-doped, yttrium lithium fluoride crystal Ho^{3+}:YLF laser at $\lambda = 2.051\ \mu m$ wavelength was parametrically converted to the Mid-IR, $\lambda = 3 - 6\ \mu m$ wavelength employing nonlinear $ZnGeP_2$ crystals in Ref. [20].

These emission wavelengths can be nowadays obtained directly via a number of sources such as ICLs or QCLs. These kinds of lasers are also exploited for environmental monitoring [21–25]. The strength of the rare earth doped fiber lasers lies in their high beam quality without the drawbacks related to further fiber coupling/pigtailing.

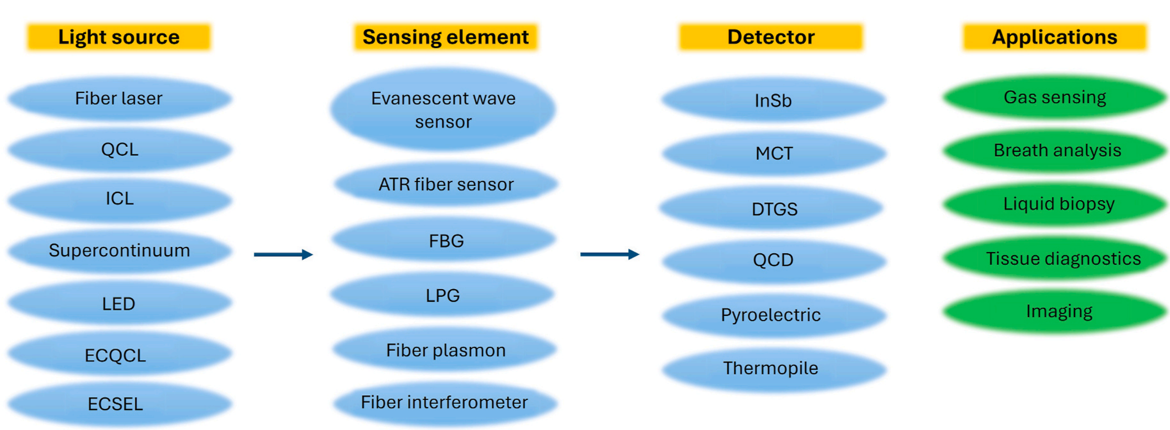

Fig. 1. A schematic overview of the possible light sources, optical fiber sensors and detectors that can be employed for Mid-IR applications.

3. Mid-IR imaging

Optical coherence tomography (OCT) in the Mid-IR wavelength range has attracted strong interest during the last decade. This technique is based on low-coherence interferometry to obtain a two-dimensional image, via the measurement of optical scattering originated by the interaction of optical beams with internal biological tissues. OCT is employed for cross-sectional imaging in biological systems with reduced invasivity. This technique allows longitudinal and lateral spatial resolutions very useful for actual applications, of the order a few micrometers. Moreover, it allows to detect very low reflected beams having power of the order of 10^{-10} of the incident power level. OCT nowadays is well known, being demonstrated e.g. in the peripapillary area of the retina such as in the coronary artery [26]. OCT is a valid technique not only for diagnostics but also to guide endoscopic laser surgery and find various excellent non-destructive applications as example in the fields of cultural heritage protection and industrial inspection [27].

The employment of Mid-IR optical sources, instead of the conventional ones at near infrared wavelengths, allows complementary images, one dimensional 1D, two dimensional 2D or three-dimensional 3D, depending on the scanning procedures, at alternative depths with respect to those obtained at conventional wavelengths of the near infrared lasers. A schematic of an OCT set-up is illustrated in Fig. 2 [28]. The most common OCT configuration employes the Michelson interferometer, based on beam splitting the light, e.g. via a 3-dB coupler, part into a sample arm and part into a reference arm, followed by another coupler allowing the interference [29]. Alternative configurations may use optical circulators, ad-hoc designed couplers, or heterodyne optical detection stages. The starting version was the Time-Domain OCT (TD-OCT), where the reference arm is mechanically scanned to change the optical path of the light by displacing the reference arm mirror, thus obtaining a time-varying delay. Then, the Swept Source (SS-OCT) and Spectral Domain (SD-OCT) versions have been developed [30,31]. The former one employes a tunable laser combined with a detector; the latter employes a broadband light source with a spectrometer at the interferometer output. More recently, the polarization-sensitive optical coherence tomography (PS-OCT) has been investigated [32]. It is based on the measurement of the birefringence of the biological tissue. Indeed, several tissues among which tendons, muscles, cartilages are characterized by specific birefringence degree, due to their sub-cellular fibrous structures which are arranged in peculiar ways/directions. A damaged or necrotized tissue exhibits a degenerated/altered structure with a lowered birefringence, the value of which indicates the degree of tissue damage. PS-OCT can employ polarization maintaining (PM) optical fibers [33–35], in this way obtaining polarization maintaining optical coherence tomography (PM-OCT). This technique can improve image contrast and detect the distribution of birefringence at higher levels, not provided by conventional OCT.

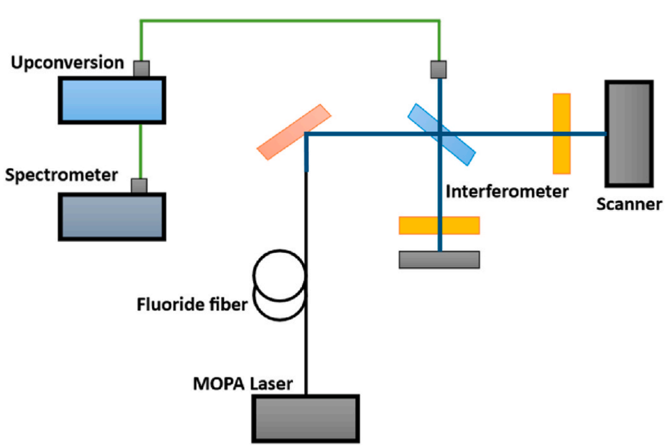

Fig. 2. An example of OCT set-up consisting of five parts that are connected via optical fiber: a broadband source (e.g. based on MOPA pump laser and fluoride fiber), a Michelson interferometer, a scanning x-y translation stage, a frequency upconversion module, and a spectrometer [28].

In [33], a novel chalcogenide photonic crystal fiber (PCF), made of glass with composition $Ge_{10}As_{22}Se_{68}$ and a transversal section allowing high birefringence, was designed and fabricated. This PCF exhibited extinction ratio, near-zero dispersion, low loss, and excellent polarization-maintaining behavior. To obtain these results, the preforms were prepared by computerized numerical control (CNC) machine, operating with high precision, allowing to reproduce the designed structure very well. The obtained birefringence was of about 10^{-4} at the wavelength $\lambda = 2\,\mu m$ and 10^{-3} at the wavelength $\lambda = 4\,\mu m$, the dispersion of about $D = \pm 1\, ps \times nm^{-1} \times km^{-1}$ in the Mid-IR wavelength region.

The feasibility of the potential applications is also related to the other PCF characteristics, including, as an example, a minimum loss of about $0.63\, dB/m$ at $\lambda = 6\,\mu m$, the average bending strength of about $240.73\, MPa$, the very high ER close to $-17.11\, dB$. This kind of fiber could be successfully employed in Mid-IR optical coherence tomography OCT systems.

4. Recent advances in Mid-IR optical fibers/materials

To achieve low-loss optical transmission, a range of glass matrices can be employed, including heavy metal oxide glasses (e.g., tellurite and germanate), non-oxide glasses (e.g., fluorides and chalcogenides), and silicon core fibers featuring a silica cladding [36,37]. These glasses have attracted a strong interest as alternative media for the transmission of optical beams beyond the spectral limits of silica glass that suffers from strong absorption losses beyond the wavelength $\lambda = 2\,\mu m$ [38–41]. Fluoride glasses can efficiently guide the light in the Mid-IR wavelength region, typically up to $\lambda = 4.5$–$5.5\,\mu m$ and chalcogenide till $\lambda = 20\,\mu m$ wavelength. The aforesaid transmission windows open the way to a number of applications. However, both chalcogenide and fluoride glass present some advantages and drawbacks. Fluoride glasses in comparison to silica glasses exhibit high sensitivity to moisture, a reduced mechanical strength and low thermal stability. These two last aspects have limited their exploitation. Chalcogenides can be employed at longer wavelength but generally with higher optical losses and exhibit lower thresholds to optical damage. However, fluoride glasses are characterized by having wider bandwidth than that of silica glasses, lower attenuation than that of chalcogenides in the $\lambda = 2$–$5\,\mu m$ wavelength range and can host rare-earth dopants with high solubility degree for active fiber applications [20]. The fabrication of chalcogenide and fluoride optical fiber requires the employment of high-purity raw materials and accurate handling procedures to minimize crystallization and reduce the losses. Furthermore, germanate glasses constitute promising media to obtain active devices operating in the Mid-IR, due to their high rare-earth solubility, low phonon energy approaching that of fluoride glasses, $\sim 900\, cm^{-1}$ for germanate and $\sim 500\, cm^{-1}$ for fluoride, and high damage threshold, which also justifies its use for endcapping in high-power lasers [36,42,43]. For instance, germanate-tellurite glass doped with Er^{3+} has allowed emission at the wavelength $\lambda = 2.7\,\mu m$ [44], while Tm^{3+}-doped germanate fibers have been investigated for emission in the eye-safe band around $\lambda = 2.0\,\mu m$ [45,46]. Table 1 presents a comparison summarizing some key physical and optical properties of silica and of the glasses capable of transmitting in the Mid-IR range [40,47–56]. The listed values are typical ones, as the precise values depend on the specific composition and elemental concentrations within each glass.

Recently, large progress has been made in the development of optical fiber Mid-IR components and devices. The recent technology allows the construction of single-mode and multimode fibers; Mid-IR optical sources and amplifiers obtained by rare-earth doping chalcogenide or

Table 1
Typical parameters of Mid-IR optical fibers.

Glass	Refractive index @ 1.55 μm	Transparency range fiber	Glass transition temperature T_g	Thermo-optic coefficient dn/dT	Thermal expansion coefficient α
Silica	1.44 [40]	$0.2 - 2.1\ \mu m$ [40]	1200 $°C$ [51]	$12 \times 10^{-6}\ 1/°C$ [51]	$0.55 \times 10^{-6}\ 1/°C$ [51]
ZBLAN	1.49[40]	$0.5 - 4.5\ \mu m$ [51]	265 $°C$ [51]	$-14.75 \times 10^{-6}\ 1/°C$ [51]	$17.2 \times 10^{-6}\ 1/°C$ [51]
Indium Fluoride	1.48[53]	$0.5 - 5.5\ \mu m$ [53]	275 $°C$ [53]	$\approx -12 \times 10^{-6}\ 1/°C$ [53]	$18 \times 10^{-6}\ 1/°C$ [53]
Germanate	1.83[52]	$0.3 - 6\ \mu m$ [54]	390 $°C$ [54]	$9 \times 10^{-6}\ 1/°C$ [52]	$10.9 \times 10^{-6}\ 1/°C$ [52]
Tellurite	2.03[40]	$0.5 - 4.5\ \mu m$ [40]	305 $°C$ [48]	$-16.4 \times 10^{-6}\ 1/°C$ [55]	$\approx 16 \times 10^{-6}\ 1/°C$ [49]
As_2S_3	2.5[40]	$1.0 - 6.0\ \mu m$ [40]	187 $°C$ [56]	$9 \times 10^{-6}\ 1/°C$ [50]	$25 \times 10^{-6}\ 1/°C$ [50]
As_2Se_3	2.9[40]	$1.5 - 9.0\ \mu m$ [40]	193 $°C$ [47]	$\approx 32 \times 10^{-6}\ 1/°C$ [47]	$22 \times 10^{-6}\ 1/°C$ [47]

fluoride fibers; supercontinuum generation by exploiting the nonlinearities overall in chalcogenides; the construction of fiber Bragg gratings (FBG), long period gratings (LPG), specialty fiber components designed for astronomical applications, and interferometric sensors [39–41,57].

However, further progress is still required to find on the market several of the Mid-IR optical fiber systems promised by the research investigation. As an example, a complete procedure standardization via well-defined fabrication protocols of splicing techniques, with the aim of obtaining high quality, low-loss, high-feasibility fiber connections is still challenging for fluoride glasses. Moreover, a set of key devices are required for the construction of actually operating Mid-IR systems. For instance, Mid-IR optical isolators, useful to protect optical systems from back reflections; fiber combiners and couplers to be employed in complex optical circuitry; tapered fiber and LPG for sensing; FBG as mirror to be integrated in optical fiber laser cavity, remain all intriguing research topics. True commercial and industrial applications need the integration of active Mid-IR fibers in systems requiring strong improvements in thermal handling, long-term operational stability, mechanically robust packaging.

5. Mid-IR optical sources

5.1. Mid-IR sources based on non-linear phenomena in optical glasses

Environmental, structural and human health monitoring often needs optical systems based on optical fibers and optical sources handling wide range of wavelengths, as seen for OCT imaging technique. Despite the impressive literature production, for shortness, only few Mid-IR sources based on NL phenomena are here recalled as examples, with reference to the recent literature.

By exploiting the transparency properties of silica, fluoride, and chalcogenide based NLFs, Mid-IR supercontinuum generation can be efficiently obtained via a cascade nonlinear fibers (NLFs) [58–60]. In particular, these glasses can provide nonlinear and dispersion behavior in different regions. The transparency spectral region of chalcogenide includes that of fluorides and the transparency spectral region of fluorides includes that of silica. Thus, a collective transparency behaviour can be imagined for a system made by the cascade of three different optical fibers. A short pump pulse, having duration of nanosecond-to-picosecond is delivered into a first silica NLF. The pulse, due to the modulation instability splits into thousands of fundamental solitons. These fundamental solitons have short durations and high peak powers. In this first stage, a first soliton self-frequency shift (SSFS) occurs. In the second fluoride NLF, solitons are in the anomalous dispersion regime and, through a fission mechanism, generate several fundamental solitons. In this way, a further SSFS is obtained. As a consequence, at the output, a high number of solitons, spread in time and wavelength are obtained. This mechanism allows to achieve a supercontinuum generation (SCG) characterized by having a broad and flat spectrum. In Ref. [61], a pump pulse at a wavelength $\lambda = 1.94\ \mu m$ with an energy of 10.6 nJ was sent in the first silica fiber stage providing tunable solitons at longer wavelengths up to $\lambda = 2.14 \mu m$. A ZBLAN NL fiber was employed as second stage, providing solitons at the wavelength of $\lambda = 2.52\ \mu m$. The chalcogenide fibers provided the third SSFS providing solitons at the wavelength of $\lambda = 3.28\ \mu m$. The set-up employed for this experiment is illustrated in Fig. 3.

An alternative technique to obtain optical sources of actual interest is based on the Stimulated Raman scattering of chirped ultrashort pulses in gas-filled hollow-core (GFHC) fibers. Recently, Raman gas filled laser (GFL) for emission of nanosecond pulses at wavelengths up to $\lambda = 4.42\ \mu m$ have been reported in literature [62–67]. The strength point of this technique is the capability to obtain a direct wavelength conversion of easily available near-infrared pulsed lasers outputs directly into the Mid-IR wavelength region. In Ref. [62], Stimulated Raman scattering obtained via chirped picosecond pulse at the wavelength $\lambda = 1.03\ \mu m$ in a hollow-core fiber filled with Hydrogen/Deuterium (H_2-D_2) gas-mixture is reported. A Mid-IR gas fiber Raman laser providing emission at the wavelengths of $2.68\ \mu m$, $3.23\ \mu m$, $3.9\ \mu m$, $4.08\ \mu m$ and supercontinuum generation with spectral covering up to $\lambda = 4.2\ \mu m$ was demonstrated. Moreover, a high-power Mid-IR Raman laser with a tunable wavelength range from about $\lambda = 2850\ nm$ to about $\lambda = 2920\ nm$ was obtained in Ref. [68] by employing a D_2 deuterium-filled hollow-core fiber. The pump beam at the wavelength $\lambda = 1545\ nm$ was provided by a tunable high-power pulsed erbium-doped fiber amplifier. A very high average power of about $P = 6\ W$ was demonstrated with a conversion efficiency of about $\eta = 14\%$ with respect to the output power of the pump source.

The exploitation of SCG technique is of strong interest not only for OCT applications but also for more conventional monitoring approach as the evanescent field sensing. This explains the recent strong interest and the related large literature production [58,69–76]. Different NL fibers have been investigated obtaining interesting results, sometime to be better evaluated by considering the SC power stability, as example corresponding to the root-mean-square (RMS) of the power in a fixed operation time. In Ref. [58], a SC laser was obtained with a piece of chalcogenide fiber (As_2S_3/As_2Se_3) pumped at the wavelength $\lambda = 1.56\ \mu m$ by a Master Oscillator Power Amplifier (MOPA) system and covering the spectral range from $\lambda = 1.5\ \mu m$ to $\lambda = 10.5\ \mu m$, providing a very good stability measured for a week with 8–9 h operation daily. In Ref. [69], a piece of ZBLAN fiber was employed for obtaining a flat spectral range from $\lambda = 1.9\ \mu m$ to $\lambda = 3.68\ \mu m$, as illustrated in Fig. 4. In Ref. [70], a high-power flat Mid-IR supercontinuum source was obtained by employing a piece of Ultra-High NA Silica Fiber UHNA7 fiber which

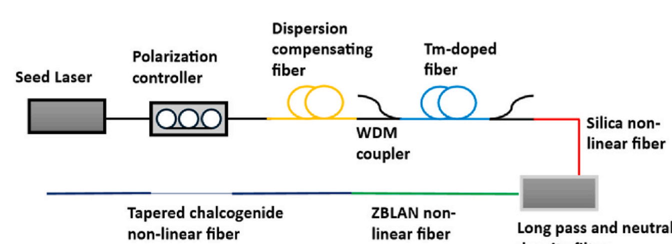

Fig. 3. Scheme of a set-up used for wavelength conversion via the exploitation of silica, fluoride and chalcogenide cascade [61].

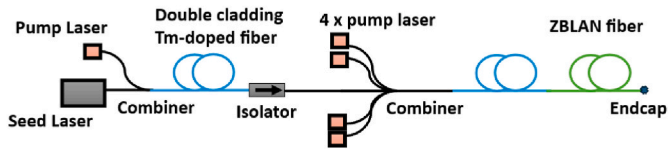

Fig. 4. Scheme of a set-up used for achieving spectrally flat Mid-IR supercontinuum pumped via 2 μm noise-like pulse MOPA [69].

was pumped by $1.9-2.6\ \mu m$ supercontinuum laser. The obtained source has exhibited a light spectrum from $\lambda = 1.77\ \mu m$ to $\lambda = 3.31\ \mu m$ wavelength and a maximum average output power of about $P = 12\ W$. This result was reached by optimizing the seed pulse parameters and the NL fiber length, thus obtaining a SC source providing high-power and flatness based on a low GeO_2 doped fiber.

5.2. Rare earth doped optical fiber lasers

Rare earth doped optical fiber lasers in Mid-IR are challenging and constitute a hot topic for research and industry. Those based on fluoride and chalcogenide fibers can enable long wavelength emission, high optical gain, and high beam quality [77,78]. Although chalcogenide glasses allow excellent Mid-IR transparency, i) the reflection losses in free propagation at fiber end facets, due to high refractive index, and ii) the propagation losses in some bands, such as around $\lambda = 4\ \mu m$, can limit their employment for some specific applications [79]. As a possible alternative, fluoride-based optical fibers, particularly ZBLAN and fluoroindate, have been investigated. Their low phonon energy, reduced attenuation, and low nonlinear properties make them promising candidates for Mid-IR lasing in active fibers [80].

Fig. 5 shows the schematic of a typical optical fiber laser. The pumping light is delivered via a pump combiner, into the inner cladding of the rare-earth doped optical fiber. The multiple fiber section allows to increase the pump power level. The laser cavity is obtained by means of FBGs, spliced to the active fiber. In the last section, the laser high quality beam is delivered for its exploitation.

Several experimental Mid-IR spectroscopical studies and laser designs, have predicted the potential of devices when based on fluoride fibers, highlighting the possibility of achieving stable laser emissions and efficient amplification in this spectral region. This is also confirmed by a number of laser fabrications reported in literature. Various rare-earth ions, including erbium (Er^{3+}), dysprosium (Dy^{3+}), holmium (Ho^{3+}), thulium (Tm^{3+}), and praseodymium (Pr^{3+}), exhibit characteristic emission bands in the Mid-IR, covering wavelengths from approximately $\lambda = 2\ \mu m$ to $\lambda = 5\ \mu m$.

Fig. 6 reports the main Mid-IR emissions in rare earth ions, under different pumping conditions, for fluoride fibers. The secondary pumping wavelength, for dual-pumping schemes, is depicted in blue, while cascade lasing is reported in orange. It also reports multiphonon decays (MP) and the main second order phenomena, i.e. cross-relaxation (CR), energy transfer upconversion (ETU).

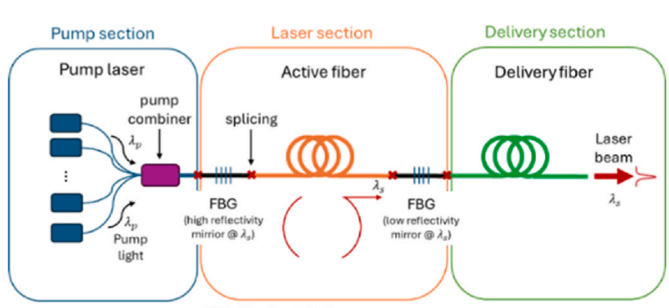

Fig. 5. Scheme of a fiber laser.

5.2.1. Emission between 2 μm and 3.5 μm

To achieve emission at $\lambda = 2\ \mu m$ and beyond, different rare earths can be considered as dopants. As an example, Tm^{3+} ions, when incorporated into fluoride fibers, enable lasing near the wavelengths $\lambda = 1.9\ \mu m$, ($^3F_4 \rightarrow {}^3H_6$) and $\lambda = 2.3\ \mu m$, ($^3H_4 \rightarrow {}^3H_5$). In Ref. [81], a Tm:ZBLAN has been pumped by a tunable Ytterbium (Yb) fiber laser around $\lambda = 1.05\ \mu m$ to generate output power $P = 1.24\ W$, in the wavelength range $\lambda = 2269-2282\ nm$ with a slope efficiency of $\eta = 37\%$ in the quasi-continuous-wave regime.

Strong Mid-IR emission in the wavelength range $\lambda = 2.7–2.9\ \mu m$ can be obtained by considering erbium-doped fibers due to transition $^4I_{11/2} \rightarrow {}^4I_{13/2}$ in Er^{3+}:ZBLAN and Er^{3+}:InF_3, under $\lambda = 980\ nm$ excitation [82–86]. It is one of the most investigated transitions thanks to the commercial availability of pumping laser diodes in the range $\lambda = 975-980\ nm$. To increase the system efficiency, cascade lasing schemes have been investigated, involving the transitions $^4I_{11/2} \rightarrow {}^4I_{13/2}$ for the emission at the wavelength $\lambda = 2.8\ \mu m$ and $^4I_{13/2} \rightarrow {}^4I_{15/2}$ at the wavelength $\lambda = 1.6\ \mu m$ [82].

Thanks to the Excited State Absorption (ESA) phenomenon $^4I_{13/2} \rightarrow {}^4I_{9/2}$, pumping at $\lambda = 1.7\ \mu m$ can be considered a feasible alternative to pumping at the wavelength $\lambda = 980\ nm$, allowing the slope efficiency of about $\eta = 23.7\%$ [83]. As an alternative, a fiber laser based on a Er:ZBLAN glass, under dual pumping at the wavelengths $\lambda = 976\ nm$ and $\lambda = 1.7\ \mu m$ has been fabricated to achieve total slope efficiency $\eta = 33\%$ [84].

Similar emission wavelength around $\lambda = 2.86\ \mu m$ can be also obtained by exploiting Ho^{3+}-doped fibers, via a pump at the wavelength $\lambda = 1150\ nm$. To improve the slope efficiency, dual-pumping techniques at $\lambda = 1642\ nm$ and $\lambda = 1976\ nm$ or Ho^{3+}/Pr^{3+} co-doping solutions have been successfully explored [87,88]. Both approaches aim to produce a stronger self-circulatory system in comparison with the conventional Ho^{3+}-doped $\lambda = 1150\ nm$ single-wavelength pumping system. Dual-pumping excitation, at the wavelength $\lambda = 1976\ nm$, and $\lambda = 1642\ nm$, in a Ho^{3+}-doped fluoroindate fiber has enabled output power $P = 1.65$ W, with slope efficiency $\eta = 53.7\ \%$ with respect to the launched pump power at the wavelength $\lambda = 1642\ nm$ and an overall optical efficiency of $\eta = 33.3\ \%$. Moreover, this dual-wavelength pumping scheme suggests the possibility to create $\lambda = 3.9\ \mu m$ and $\lambda = 2.9\ \mu m$ cascade lasers in lightly Ho^{3+} doped fluoroindate glass fiber [88]. Other literature investigations have demonstrated Dy^{3+}-doped ZBLAN fiber lasers tunable from the wavelength $\lambda = 2.8\ \mu m$ to $\lambda = 3.4\ \mu m$ when pumped at the wavelength $\lambda = 1.7\ \mu m$, achieving output powers up to $P = 170\ mW$ with a $\eta \approx 21\%$ slope efficiency [89]. Dy:ZBLAN has been employed also to obtain emission at $\lambda = 3.2\ \mu m$ with high output power and slope efficiency [90,91]. For emission around $\lambda = 3.44\ \mu m$, erbium-doped fibers have been investigated, due to the transition $^4F_{9/2} \rightarrow {}^4I_{9/2}$. A tunable laser in the range $\lambda = 3.25-3.91\ \mu m$ has been proposed in erbium-doped fluoroindate fibers, by exploiting the same transition and pumping at $\lambda = 635\ nm$ [92]. Simulation results show emission bandwidth $BW = 659\ nm$, obtained for the laser with a low threshold, $P_{th} = 25\ mW$, with the maximum output power is $P = 15.5\ mW$. The same transition in erbium-doped fluoride fibers has been considered for the design of ultrafast pulsed lasers, with stable femtoseconds pulses at a the wavelength $\lambda = 3.4\ \mu m$ [93]. Moreover, a dual-pumping scheme at both $\lambda = 974\ nm$ and $\lambda = 1976\ nm$ has been proposed to increase slope efficiency [94–96].

Co-doping strategies have been employed to mitigate non-radiative losses in oxide glasses and enhance emission efficiency within the near- and lower-mid-infrared range.

Among the most common co-doped systems is Yb^{3+}/Er^{3+}, where Yb^{3+} serves as a sensitizer absorbing pump light around 980 nm and for energy transfer to Er^{3+} ions, which can emit near 1.5 μm and, with proper energy management, around 2.7–2.9 μm via the $^4I_{11/2} \rightarrow {}^4I_{13/2}$ transition. This strategy enhances pump absorption and suppresses ion

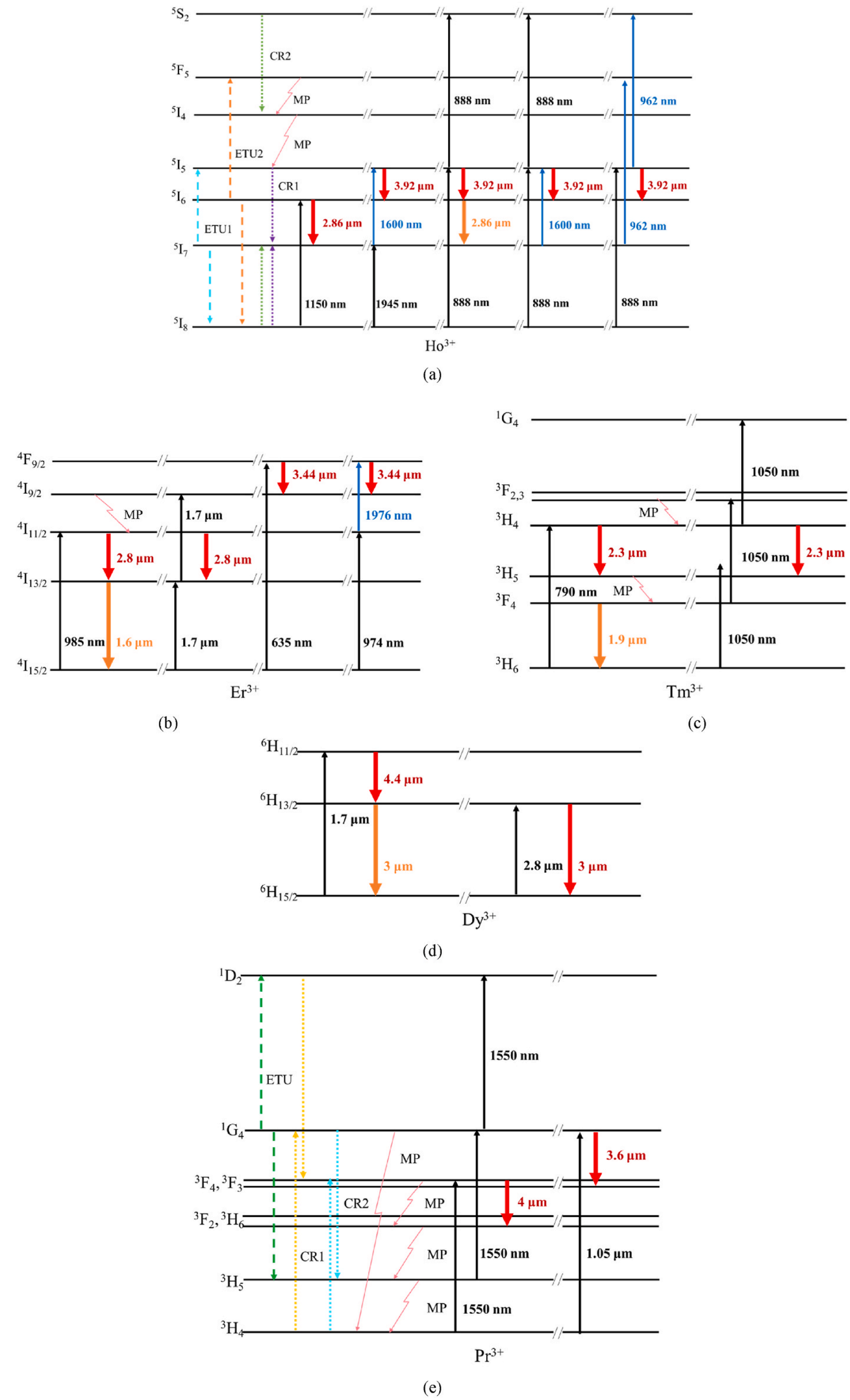

Fig. 6. Main Mid-IR emissions in rare earth-doped fluoride fibers with different pumping schemes: (a) holmium, (b) erbium, (c) thulium, (d) dysprosium, (e) praseodymium. Including: multiphonon (MP) decays (pink lightning arrow), cross-relaxations (dotted arrows), energy transfer upconversion (dashed arrows), secondary pumping (blue solid arrows), and cascade lasing (orange solid arrows).

clustering, with increased pump-to-signal efficiencies around 34–37 % [97]. $Er^{3+}/Ce^{3+}/Yb^{3+}$ triply-doped bismuth borosilicate glasses leverage Ce^{3+} to suppress up-conversion, improve mid-IR emission efficiency, and broaden bandwidth [98]. In tellurite and bismuthate glasses, for which the phonon energies are lower than that of the silica glasses, co-doping combinations such as Er^{3+}/Tm^{3+} or Ho^{3+}/Yb^{3+} have been used to facilitate cascade lasing and broaden the gain bandwidth.

In non-oxide low-phonon hosts like chalcogenide and fluoroindate glasses, deeper mid-IR transitions become feasible. Pr^{3+}/Dy^{3+} co-doping in selenide-chalcogenide fibers, when pumped at 1320–1700 nm, has permitted to obtain ultra-broadband photoluminescence spanning 2–6 µm, with spectral shaping achieved via pump wavelength selection [99].

Similarly, Pr^{3+}/Ho^{3+} systems, pumped near 1 μm, enable efficient emission beyond 3 μm range [100].

Fig. 7 summarizes some important achievements obtained in Mid-IR continuous wave (CW) lasers based on fluoride fibers, emitting between $\lambda = 2\ \mu m$ and $\lambda = 3.5\ \mu m$, taking into account output signal power and slope efficiency.

5.2.2. Emission between 3.5 μm and 5 μm

Ho^{3+}-doped fibers can be exploited for emission till $\lambda = 3.9\ \mu m$, considering the transition $^5I_5 \rightarrow {}^5I_6$. To this aim, fluoride fibers have been widely investigated. Recently, an all-in-fiber CW laser has been fabricated, reaching the output power $P = 1.7\ W$ at the wavelength $\lambda = 3.92\ \mu m$ when pumped at $\lambda = 888\ nm$. It is based on a heavily-doped double-cladding fluoroindate fiber and integrated FBGs to obtain the laser cavity. The obtained slope efficiency was $\eta = 9.2\ \%$ and input power threshold $P_{th} = 30\ W$ [101]. Based on the same fiber, a gain-switching pulsed laser has been proposed via simulation, predicting output peak power $P_s^{peak} = 14.62\ W$ with repetition rate $f = 100\ kHz$ [102]. With the aim of increasing the slope efficiency and reducing the input pump threshold, other dual-pumping or co-doping strategies have been investigated. As reported in Fig. 6, a second pump at the wavelengths $\lambda = 976\ nm$ or $\lambda = 1660\ nm$ have been proposed [103–105]. Co-doping with neodymium has been explored under pumping at $\lambda = 808\ nm$. Thanks to energy transfer (ET) phenomena, the self-termination of the transition $^5I_5 \rightarrow {}^5I_6$ was avoided, allowing the slope efficiency to increase up to $\eta = 16.67\ \%$ and reducing the input power threshold to $P_{th} = 0.2\ W$ [105].

Recently, by considering dual pumping at $\lambda = 1660\ nm$ and $\lambda = 1945\ nm$, a CW laser based on $Ho:InF_3$ has been simulated, reducing the input power threshold to $P_{th} = 1.6\ W$ [106].

An alternative for emission at the wavelength $\lambda = 4\ \mu m$ lays in praseodymium-doped fluoroindate fibers, by considering $^3F_4 \rightarrow {}^3H_6$ transition, under near-infrared excitation at $\lambda = 1550\ nm$. This possibility has been explored via simulation in Ref. [107]. Also co-doping solutions have been investigated for emission at $\lambda = 3.6\ \mu m$. By exploiting the $^1G_4 \rightarrow {}^3F_4$ transition in ZBLAN fibers, it is possible to pump the system at $\lambda = 970\ nm$. Moreover, Dy^{3+}-doped fluoroindate fiber lasers have been designed for emitting at wavelength $\lambda = 4.4\ \mu m$, when pumped at $\lambda = 1.7\ \mu m$ [108,109], showing slope efficiency $\eta \approx 27\ \%$ and high pump power threshold $P_{th} \approx 30\ W$, for the CW laser with cascade emission at wavelengths $\lambda = 3.3\ \mu m$ and $\lambda = 4.4\ \mu m$.

Fig. 8 summarizes some important advances obtained in Mid-IR CW lasers based on fluoride fibers, emitting between $\lambda = 3.5\ \mu m$ and $\lambda = 5\ \mu m$, taking into account output signal power and slope efficiency.

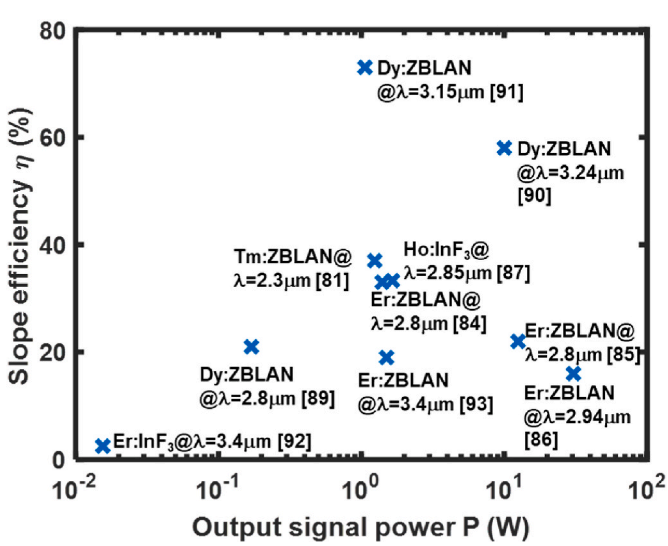

Fig. 7. Some important achievements obtained in Mid-IR CW lasers based on fluoride fibers, emitting between $\lambda = 2\ \mu m$ and $\lambda = 3.5\ \mu m$.

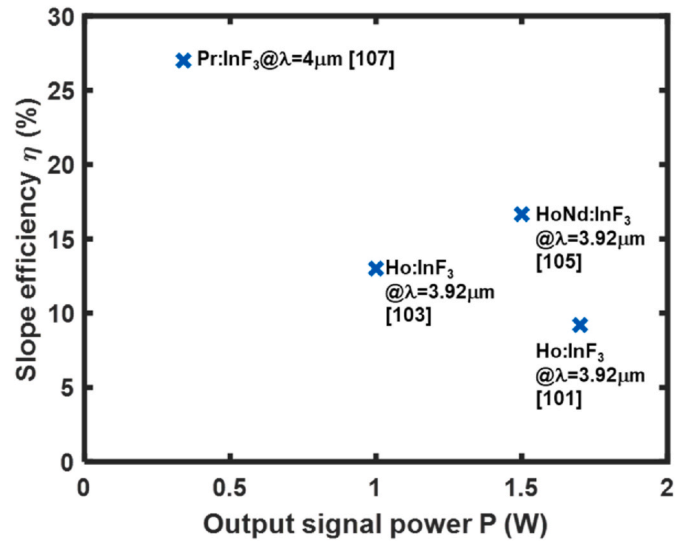

Fig. 8. Some important advances obtained in Mid-IR CW lasers based on fluoride fibers, emitting between $\lambda = 3.5\ \mu m$ and $\lambda = 5\ \mu m$.

6. Key elements for integrated Mid-IR all in fiber systems

6.1. Optical fiber combiners

Optical fiber combiners play a crucial role in enabling power scaling, spectral beam combining, and the delivery of multiple pump sources into a single rare-earth doped fiber. The ability to efficiently combine multiple pump or signal sources through a compact and low-loss optical fiber combiner is essential for achieving the high output power and beam quality required by practical systems [110]. In other words, the use of the optical fiber opens the door to scalable Mid-IR fiber systems, enabling both wavelength and power scaling without relying on bulky free-space optics or complex alignment-sensitive components. However, fabricating combiners based on fluoride glass presents numerous difficulties, due to the need for precise tapering and fusion splicing techniques that allow to preserve the integrity of the soft glass material [111].

The most widely employed fabrication method for silica fiber combiners is the fused taper technique, illustrated in Fig. 9 [112]. The process begins with the cleaving of segments of the input fibers, which are then inserted into a low refractive index silica capillary tube. The capillary acts as a structural support, ensuring uniform tapering. The entire assembly is locally heated using a resistive filament, a flame or a CO_2 laser. As the assembly softens, it is pulled to create a fused biconical taper. This technique can also be employed for the fabrication of combiners based on fluoride fibers; however, several critical differences must be considered due to the inherent properties of fluoride glass. Unlike silica, fluoride glasses are significantly softer, have lower melting points, and are much more sensitive to thermal and environmental conditions. As a result, the fabrication temperature must be carefully reduced to avoid crystallization or structural damage [113]. Moreover, the processing window for each fabrication parameter, such as heating rate, and pulling speed, is considerably narrower than those employed for in silica-based fabrication. This makes the fluoride fabrication process far more delicate and requires precise thermal control and a highly controlled environment to ensure reproducibility in the geometry and in the optical performance.

Despite these challenges, a fully fluoride-based fiber combiner has recently been realized, marking a significant advancement in Mid-IR

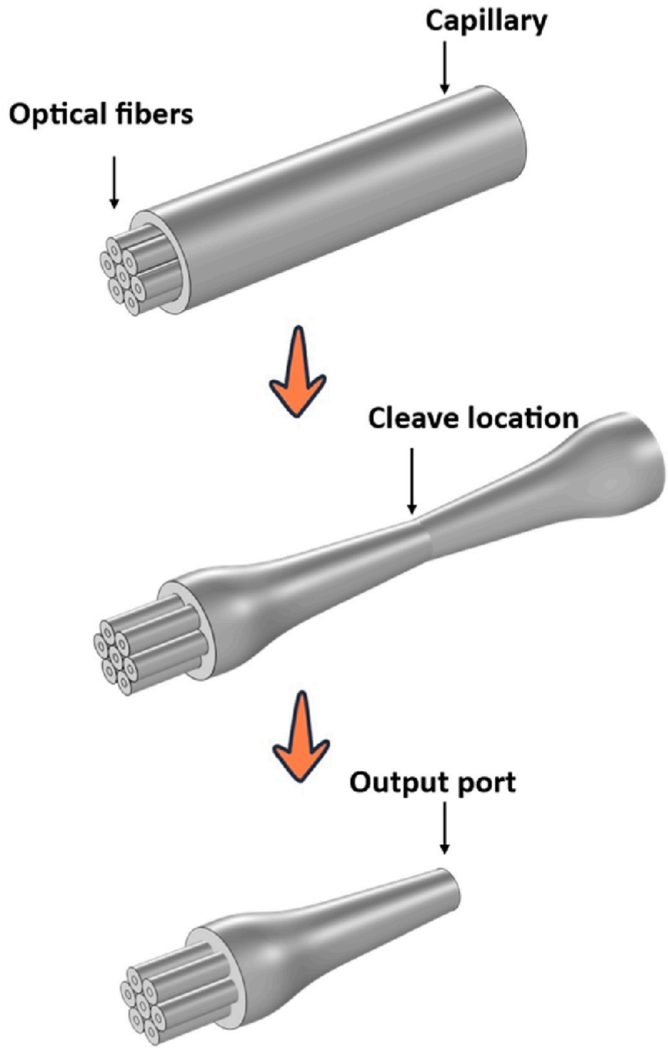

Fig. 9. Illustration of the optical fiber combiner fabrication process: multiple optical fibers are inserted into a glass capillary; a fused biconical taper is formed through precise heating and stretching; the output port is created by cleaving the taper at its narrowest (waist) region.

fiber technology, although it has not yet been tested under high-power operation [114]. In this demonstration, three multimode step-index fibers were precisely arranged within an indium fluoride glass capillary. The assembly was uniformly heated using a graphite filament and tapered to form a smooth, low-loss transition from three multimode inputs to a single multimode output. The fabrication was carried out using a Vytran glass processing system. Both numerical modeling and experimental measurements were conducted to validate the device operation across a broad spectral range, extending up to $\lambda = 5.00\ \mu m$. The measurement confirmed the expected flat spectral response. This component not only unlocks new possibilities for power scaling and system integration but also serves as a critical enabler for in-band pumping strategies, which are essential for maximizing efficiency and aiming at lasing at longer wavelengths.

Moreover, fluoride fiber combiners hold significant promise not only for the development of all-fiber high-power laser systems but also for advanced Mid-IR sensing applications. Recently, a fluoride-based fiber combiner has been employed to merge two distinct Mid-IR wavelengths, i.e. $\lambda = 4234\ nm$ and $\lambda = 5263\ nm$, targeted for the detection of carbon dioxide (CO_2) and nitric oxide (NO), respectively, using quartz-enhanced photoacoustic spectroscopy (QEPAS) [25]. In the setup, the combined laser beams were delivered thanks to the fluoride combiner into a compact commercial acoustic detection module equipped with a fiber-coupled input. This architecture enabled a fully integrated, plug-and-play sensing platform with high sensitivity. The results showed enhanced detection capabilities, reaching limits of 13 ppm for CO_2 and 4 ppm for NO at an integration time $t = 10\ s$.

When all-fluoride fiber combiners need to be pumped using visible or near-infrared laser sources delivered through standard silica fibers, a hybrid connection between silica and fluoride fibers becomes necessary. In such cases, a silica-to-fluoride optical fiber splice can be employed to bridge the material gap [115,116]. A recent study has explored the feasibility of this approach, evaluating the mechanical robustness of splices between silica and fluoride fibers [117]. It is worth noting that the significant differences in the glass transition temperature T_g make direct tapering of silica and fluoride fibers inside a capillary unfeasible. Consequently, additional techniques must be employed to obtain pump delivery via silica fiber in a rare-earth doped fluoride optical fiber.

A new strategy for delivering pump light has been realized through the design of an end-coupled hybrid fiber combiner linking silica and fluoride fibers [118]. This device merges a tapered silica fiber for pump input with a double-clad fluoride fiber used for signal amplification. The system achieves around 90% coupling efficiency when powered by a multimode laser diode. The hybrid combiner has been successfully tested in Mid-IR platforms such as ultrafast fiber lasers and broadband supercontinuum sources.

An alternative technique employs side-coupling to inject pump light into fluoride-based double-clad fibers, achieving up to 93% coupling efficiency and supporting power levels near $P = 100\ W$ at $\lambda = 981\ nm$ [119].

This method bypasses the challenges of direct splicing between silica and fluoride fibers by using a tapered, coreless 125 μm silica fiber that is helically coiled around the fluoride fiber outer cladding. Light is coupled through the evanescent field, eliminating the need for complex fusion processes. Operating under passive cooling, this configuration has exhibited stable performance in both undoped and erbium-doped fluoride fibers, maintaining continuous operation for several hours at pump powers $P = 91\ W$ and $P = 44\ W$, respectively.A further advancement in hybrid coupling is found in evanescent-wave coupling via side-polished fiber geometries [120]. This approach utilizes D-shaped fibers formed by precision polishing of both silica and erbium-doped ZBLAN fibers. By aligning the flat surfaces with micrometer-scale accuracy and using refractive index matching along with thermal control, the researchers achieved pump coupling efficiencies of about 80% at $\lambda = 980\ nm$. The optimal polishing depths were empirically tuned, yielding interaction regions approximately 111 μm wide for silica and 352 μm for the active fluoride fiber. Detailed profilometry confirmed that surface finish plays a key role in enhancing power transfer across the interface.

6.2. Optical fiber coupler

Despite the inherent challenges posed by the thermal processing of fluoride glasses, including their propensity to crystallize, narrow temperature windows for processing, hygroscopicity, low glass transition temperatures, and mechanical fragility, significant progress has been achieved in the fabrication of fluoride-based optical fiber couplers with multimode, few-mode, and single-mode fibers.

One important advancement lies in the fabrication of multimode step-index indium fluoride fiber couplers, where a customized setup, featuring precise temperature control within $\pm 1^{\circ}C$ and a controlled nitrogen atmosphere, enabled a fast-tapering process [121]. This method effectively balanced the delicate viscosity and temperature parameters to avoid fiber melting and crystallization while maintaining mechanical stability during fusion and tapering steps. As a result, the process yielded fused couplers exhibiting low excess loss of only $EL = 0.35\ dB$ at a wavelength of $\lambda = 1.7\ \mu m$, with a coupling ratio of approximately $CR = 45:55$.

In the single-mode regime, the first demonstration of optical fiber couplers fabricated from ZBLAN fluoride glass fibers used a controlled multiple-sweep tapering technique that allowed for high reproducibility in fiber geometry and minimized bulk crystallization [122]. These ZBLAN couplers achieved coupling ratios up to $CR = 41 : 59$ at the wavelength $\lambda = 2.73\ \mu m$, with an excess loss $EL = 2.5\ dB$. The characterization was performed over a broad spectral wavelength range from $\lambda = 1.5\ \mu m$ to $\lambda = 3.0\ \mu m$. Long-term tests showed that these devices maintained chemical stability in atmospheric ambient conditions for more than 90 days, this highlighting their robustness for practical deployment outside laboratory environments.

The first 2×2 optical fiber coupler using few-mode indium fluoride fibers, with enhanced mechanical handling enabled by a capillary structure, was designed using coupled mode theory and fabricated via fused biconical tapering on a conventional Vytran GPX-2400 glass processing system [123].

The obtained device demonstrated excellent agreement between experimental performance and theoretical predictions, achieving a coupling ratio of approximately $CR = 70 : 30$ and an excess loss as low as $EL = 0.9\ dB$ at $\lambda = 3.34\ \mu m$. Fig. 10 illustrates the fused biconical taper region of a fluoride fiber coupler, produced through this capillary-assisted fabrication technique.

The first polarization-dependent optical fiber coupler based on ZBLAN fibers was recently demonstrated [124]. This device exhibited polarization extinction ratios $PER = 2.5\ dB$ at the through-port and $PER = 4.0\ dB$ at the cross-port, alongside a coupling ratio $CR = 73.5 : 26.5$ under unpolarized input light and a low excess loss $EL = 1.47\ dB$ at the wavelength $\lambda = 1.918$ μm. Remarkably, the coupler supported optical powers $P = 320\ mW$ without damage, highlighting its optical robustness. By exploiting its intrinsic polarization sensitivity, the coupler was integrated into a nonlinear mode-locking scheme, enabling the fabrication of an all-fiber Mid-IR laser. This system produced stable fundamental soliton pulses with durations of approximately $1.83\ ps$ at $\lambda = 1.918\ \mu m$, demonstrating the coupler effectiveness as a key functional component in nonlinear Mid-IR photonic architectures.

These developments underscore the growing maturity of fluoride fiber coupler technology, which now enables the fabrication of low-loss, high-performance components tailored for specialized applications.

6.3. Photonic lantern

Significant advances have been reported in the development of Mid-IR photonic lanterns based on indium fluoride fibers, which have promising applications in fields such as astrophotonics, thermal imaging, and Mid-IR communications [125–127]. The fabrication process usually closely follows the fused biconical tapering technique, traditionally used for fiber combiner. An example of the multimode end-face of an indium fluoride photonic lantern, comprising seven identical fiber cores, is illustrated in Fig. 11. Another photonic lantern has been constructed from two single-mode fibers and a few-mode fiber, designed for mode-selective operation at the wavelength $\lambda = 3.34\ \mu m$ [128]. The device leverages the different optical properties of constituent fibers to achieve mode-group selectivity, allowing excitation and low-loss propagation of the fundamental LP_{01} mode as well as the even and odd LP_{11} modes, with experimentally measured insertion losses below $1.3\ dB$ and $1.7\ dB$, respectively. The tapering procedure is meticulously controlled under an argon atmosphere to mitigate the hygroscopicity of fluoride glass and to prevent surface crystallization and impurity-induced nucleation.

The taper angle and length are optimized to satisfy adiabatic conditions, with a down-taper length of approximately $L_{dt} = 25\ mm$ and an average taper angle of 0.41°, ensuring minimal mode coupling loss and maintaining the integrity of mode transitions through a decaying-exponential taper profile.

In a complementary study [129], the indium fluoride mode-selective photonic lantern has been exploited to obtain a highly efficient, transverse offset-tolerant coupling, mechanism in single-mode fiber. Light is coupled in the multi-mode end of the device and then univocally guided by the fiber with the largest normalized frequency V. This structure employs three single-mode fibers with carefully optimized core diameters and an outer capillary diameter of $400\ \mu m$ to realize mode-selective excitation at $\lambda = 3.34\ \mu m$. Efficiency is directly related to two key aspects: matching the fundamental mode profile of the multi-mode end to the input beam and minimizing taper-induced losses during the fusion process. The investigation reports a measured coupling efficiency $\eta = 47\%$, highlighting the effectiveness of the design.

Increasing the number of fibers in the bundle (e.g. seven fibers) can improve the cylindrical symmetry of the beam at the multi-mode end and the coupling efficiency but it adds fabrication complexity and challenges in maintaining uniformity across the fibers.

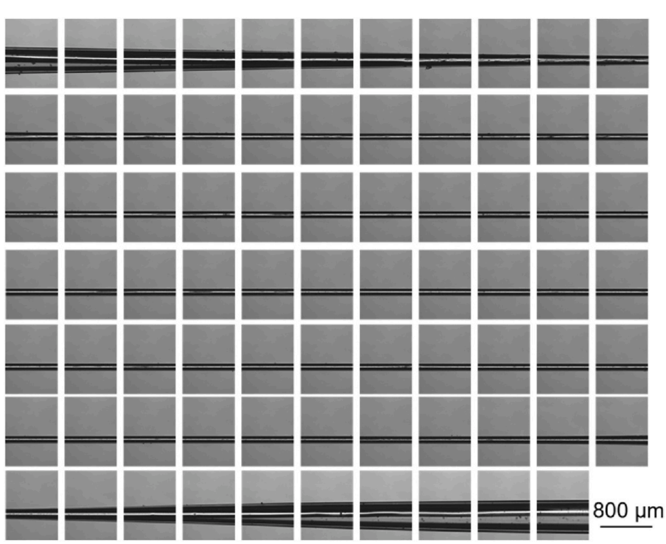

Fig. 10. Fused biconical taper showing the outer shape of the indium fluoride capillary, enclosing two indium fluoride optical fibers.

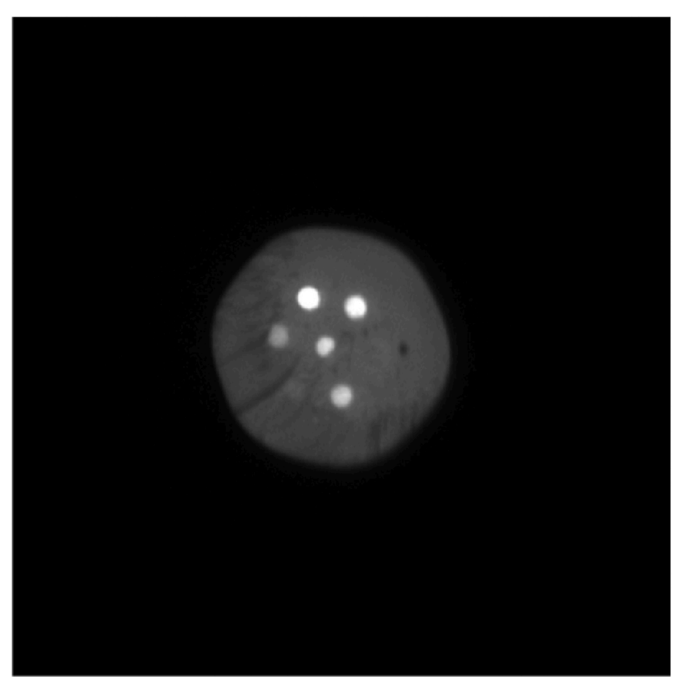

Fig. 11. Cross-section at the multi-mode end of an indium fluoride photonic lantern based on seven identical optical fibers.

6.4. Fiber gratings

The phase-mask method is among the most established and reliable techniques for inscribing FBGs. In this approach, a cylindrical lens forms the incoming laser into a narrow beam, which is then diffracted by a phase mask to produce an interference pattern [130], as sketched in Fig. 12. This pattern imprints a periodic refractive index modulation directly into the fiber core. Alternatively, the point-by-point inscription method offers considerable design flexibility, especially for engineering complex grating profiles such as chirped or aperiodic structures, usually at the cost of a slower fabrication. Here, discrete femtosecond laser pulses induce localized type-II index changes, usually manifesting as nanoscale damage sites [131]. As the fiber is translated, a grating is constructed, as shown in Fig. 12. However, this method is often accompanied by elevated scattering losses, largely attributed to Mie scattering from the abrupt microstructural features. To mitigate these drawbacks, the "continuous core-scanning" technique was introduced, maintaining the laser fluence below the damage threshold. This enables the formation of smooth, type-I index changes rather than discrete damage tracks [132]. The technique also incorporates transverse movement of the fiber, improving the mode overlap efficiency and thus the grating strength. Later, a refined "line-by-line" writing method has been proposed, to minimize cladding mode coupling, offering a more stable and reproducible FBG fabrication process [133].

For fluoride fibers, conventional UV-based inscription methods are largely ineffective, due to their low intrinsic photosensitivity, although photosensitivity can be enhanced with cerium doping [134]. A breakthrough came in 2007 with the successful inscription of FBGs into thulium-doped and undoped ZBLAN fibers using femtosecond pulses at $\lambda = 800\,nm$ [135]. Employing the phase-mask technique, the authors have fabricated gratings with an induced negative index changes on the order of 10^{-3}. Later, the same group has extended this method to highly erbium-doped double-clad ZBLAN fibers, achieving Bragg reflections near $\lambda = 2.82\,\mu m$ [136].

The first demonstration of point-by-point FBG inscription in fluoride glass has been reported by Hudson et al., in 2013 [137]. A 20 *mm*-long, first-order grating resonating at $\lambda = 2.9\,\mu m$ has been inscribed into a Ho/Pr co-doped ZBLAN fiber using a Ti:sapphire femtosecond laser operating at $\lambda = 800\,nm$. Interestingly, the refractive index modifications did not resemble the typical microvoid structures seen in silica fibers. Instead, they formed smooth, type-I index changes. This was attributed to ZBLAN lower glass transition temperature and softer mechanical properties. In 2017, the line-by-line technique has been implemented to fabricate second-order FBGs in Ho/Pr co-doped double-clad ZBLAN fibers [138]. The resulting gratings achieve $R \approx 50\%$ reflectivity and have been integrated into an all-fiber laser cavity with a slope efficiency of 17%. Notably, these gratings have been inscribed without removing the polymer coating, demonstrating both the robustness and practicality of the technique for the construction of mirrors of Mid-IR laser systems.

In another work, the employment of a two-beam phase-mask interferometer and femtosecond lasers at 266 and 400 *nm* has enabled direct-write FBG inscription in passive indium fluoride fibers [139]. These gratings exhibit notable performance, including $R > 99.7\%$ reflectivity. Post-inscription thermal annealing confirms both low insertion loss and good thermal stability.

Further innovations in FBG inscription for fluoride fibers have been reported by Zhang et al., who introduced a parallel-integrated FBG writing strategy [140]. Utilizing a burst-mode femtosecond laser operating at 1 *MHz*, they have achieved rapid and low-loss grating inscription. The high repetition rate has promoted thermal accumulation, suppressing microcrack formation and enhancing the uniformity of the refractive index modulation. The resulting ellipsoidal index profile improved mode overlap, thereby reducing insertion losses. A parallel-integrated FBG composed of three gratings has been written in just 2.5 minutes, achieving $R = 99.6\%$ reflectivity and an insertion loss as low as $IL = 0.1\,dB$. Additionally, the gratings exhibit high thermal sensitivity ($\approx 26.17\,pm/^{\circ}C$), positioning them as promising candidates for Mid-IR sensing platforms.

Finally, fluoride-based FBGs demonstrates exceptional thermal sensing performance across an extensive temperature range, starting from cryogenic conditions [141]. In contrast to silica-based gratings, which exhibit negligible thermal response at low temperatures, FBGs in fluoride fibers maintain a measurable thermal sensitivity of 0.5–1.7 pm/K even below $T = 50\,K$. This unique behaviour opens new possibilities for deploying fluoride FBGs in cryogenic sensing and extreme-environment monitoring.

LPGs have emerged as a key enabling technology in the development of Mid-IR fluoride fiber photonics, serving critical roles as spectral filters, mode converters, and gain equalizers within fiber lasers and amplifiers. Femtosecond laser inscription has proven to be an effective technique for fabricating LPGs in fluoride fibers, leveraging the precise localization and thermal accumulation effects of ultrashort pulses to induce smooth, periodic refractive index modulations [142,143]. These gratings inscribed using Ti:sapphire lasers centered around $\lambda = 800\,nm$, exhibit sharp spectral resonances with attenuation dips of $-24\,dB$ depth, and refractive index changes of the order of -3×10^{-3}. The fabrication process involves tightly focused laser pulses delivered via high-NA microscope objectives, with nanometric precision achieved through motorized translation stages and real-time camera alignment [142].

In parallel, micro-tapering has been demonstrated as an alternative approach for LPG fabrication in fluoride fibers [144,145]. Using localized heating via graphite filament elements, periodic diameter modulation has been introduced into zirconium fluoride fibers to form LPGs with grating periods between $\Lambda = 1.36\,mm$ and $\Lambda = 1.57\,mm$ [145]. These structures exhibit strong resonance dips exceeding 15 dB near $\lambda = 3.2\,\mu m$, attributed to coupling between the LP_{01} core mode and LP_{02} cladding modes. Finite element simulations and coupled-mode theory have provided accurate predictions of spectral behaviour, in good agreement with experimental results. The insertion losses at $\lambda = 2.5\,\mu m$

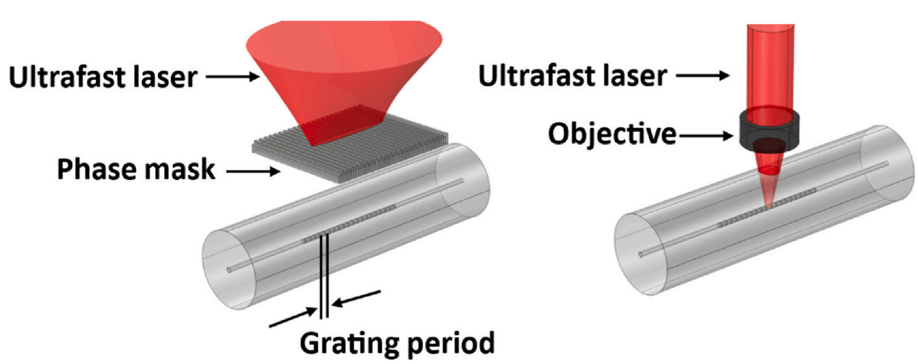

Fig. 12. Fiber grating fabrication based on phase-mask method (left) and point by point method (right).

remains acceptable, underscoring the suitability of these LPGs for high-performance Mid-IR devices. The outer shape of a longitudinal section of a micro-tapered fluoride LPG is reported in the micropictures of Fig. 13 (a), while Fig. 13 (b) reports the picture of the micro-tapered LPG.

Both femtosecond laser inscription and micro-tapering techniques offer scalable and versatile solutions for realizing high-quality LPGs in non-silica fibers—despite the intrinsic processing challenges associated with fluoride glasses. These advances not only support the suppression of parasitic lasing in supercontinuum sources and amplifiers but also enable precise control over spectral and modal properties in integrated photonic platforms. The demonstrated thermal stability, low excess loss, and strong resonance characteristics of the fluoride-based LPGs makes them highly promising for applications in Mid-IR sensing, environmental monitoring, and medical diagnostics.

6.5. All-fiber interferometers

Recent advances in the fabrication of tapered structures on single-mode ZBLAN fluoride fibers have demonstrated their efficiency as highly sensitive structures to obtain integrated Mach–Zehnder interferometric principles. These devices operate through the excitation of higher-order modes induced by a non-adiabatic down-taper or sharp bend, where core and cladding modes propagate in the taper waist and subsequently recombine, this resulting in interference patterns highly sensitive to temperature, strain, and surrounding refractive index changes [146].

The pioneering work on non-adiabatic tapered ZBLAN fibers validates the concept of leveraging fluoride glass unique thermo-optic and thermal expansion properties for enhanced temperature sensing [51]. Numerical simulations, employing 3-D beam propagation method and electromagnetic modal analysis, accurately describe the comb-like spectral response and temperature sensitivity of these tapers, predicting well the experimental results. These interferometric structures reveal a negative temperature sensitivity (blueshift of the output spectrum) contrarily to the typical positive shifts observed in silica-based tapers. This is a feature advantageous for multiparameter sensing due to improved problem conditioning and reduced cross-sensitivity. The fabrication process involved removal of the polymer coating, precision tapering using a commercial glass-processing system, and in situ monitoring of transmitted power to ensure device quality. Reported insertion losses were low, i.e. $IL \approx 0.8\ dB$ at $\lambda = 635\ nm$, indicating high-quality tapers with minimal scattering losses primarily occurring in the down-taper region. A picture of the fabricated prototype is reported in Fig. 14. Fluoride glass tapers hold several advantages over traditional silica sensors: in addition to the extended Mid-IR transparency window which allows access to molecular fingerprint regions crucial for chemical sensing, the thermo-optic coefficients remain significant even at cryogenic temperatures, where silica sensors suffer from drastically reduced sensitivity.

The first demonstration of an S-tapered fiber fabricated from zirconium fluoride glass via off-axis pulling combined with filament heating has been reported, showcasing both the feasibility and performance of such devices in the Mid-IR spectral region [147]. The picture of one of the fabricated prototypes is reported in Fig. 15. The design of these S-tapered structures was performed via three-dimensional beam propagation method simulations, which accurately predicts their spectral response and sensitivity to changes in the surrounding refractive index. This shift was systematically observed by immersing the fiber in various liquids (methanol, ethanol, propanol), demonstrating the sensor ability to distinguish between low refractive index variations in the Mid-IR wavelength range near $\lambda = 3.75\ \mu m$. The fabrication approach highlights the potential for scalable and cost-effective production of Mid-IR optical fiber sensors. The demonstrated sensitivity to surrounding RI changes highlights the potential of S-tapered fluoride fibers for environmental and biomedical sensing applications. Additional material characterization efforts, including the measurement of the glass transition temperature T_g via viscosity testing, provide precious data for understanding the thermal stability and processing windows of ZBLAN fibers.

It is worth mentioning that also other fluoride fiber sensors, e.g. those based on side-polishing, are promising for Mid-IR detection, but they are not described in this review for the sake of shortness [148].

7. Conclusion

Even if an exhaustive state of the art on Mid IR recent progress cannot be condensed in few pages, due to the impressive number of high-quality papers reported in literature, an interesting overview on the optical fibers/materials; imaging techniques, optical sources; main elements for all in fiber systems integration in Mid-IR is given. The review focuses on enabling technologies and emerging applications, illustrating the key elements for high-sensitivity applications such as chemical, biomedical, environmental sensing. Emphasis is placed on recent developments in fluoride fiber-based components that support the fabrication of compact, mechanically robust, and alignment-free, all-fiber mid-infrared systems. The integration of optical sources and systems can be clearly predicted by observing the evolution of the recalled

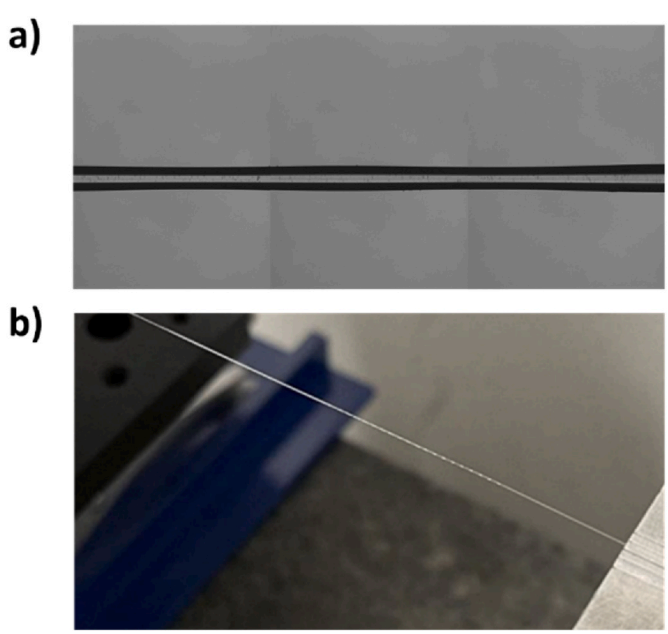

Fig. 13. a) Outer shape of a section of the fabricated zirconium fluoride LPG based on micro-tapering technique; b) Picture of a zirconium fluoride LPG based on micro-tapering technique.

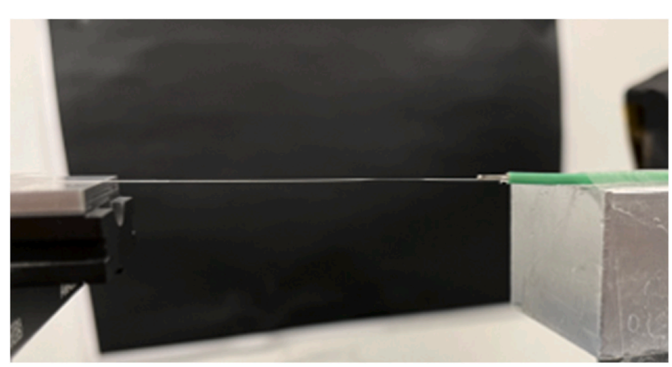

Fig. 14. Picture of a zirconium fluoride non-adiabatic taper with waist diameter $d_w \sim 25\ \mu m$ and waist length $L_w \sim 8\ mm$.

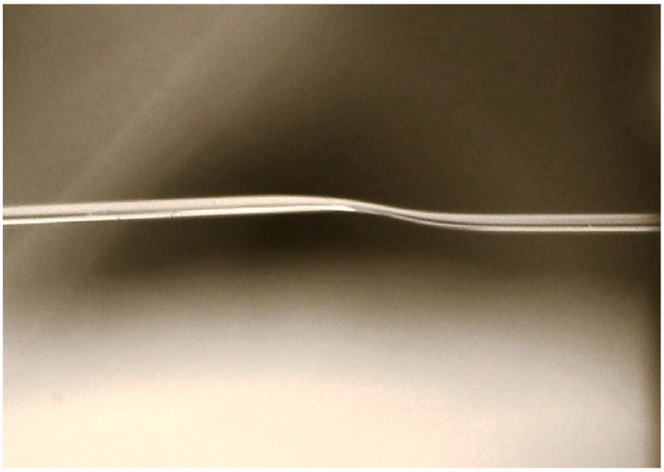

Fig. 15. Picture of a zirconium fluoride S-taper, fabricated via off-axis pulling.

results.

CRediT authorship contribution statement

Francesco Anelli: Writing – original draft, Investigation, Formal analysis, Data curation, Conceptualization. **Antonella Maria Loconsole:** Writing – original draft, Formal analysis, Data curation, Conceptualization. **Francesco Prudenzano:** Writing – review & editing, Supervision, Funding acquisition, Formal analysis, Data curation, Conceptualization.

Declaration of competing interest

The authors declare that they have no known competing financial interests or personal relationships that could have appeared to influence the work reported in this paper.

Acknowledgements

This work was partially supported by MIUR PRIN 2022, NRPP – DD n.1181 del 27-07-2023 - InnoVative tEchnoloGies for non-invasivE assessment of plAnt healTh conditIon to support precisiOn farmiNg “VEGETATION” (P2022ZF9P2, CUP: I53D23005710 001); the European Union under the Italian National Recovery and Resilience Plan (NRRP) of NextGenerationEU, with reference to the partnership on “Telecommunications of the Future” (PE00000001 - program “RESTART”, CUP: D93C22000910001) - STRUCTURAL PROJECT Antennas & Devices foR mixing, dEtection And Manipulation of mmWaves; ASI 687/2022 – MUR 341 15/03/22 “SPACE IT UP” (CUP: D53C24000570006); ASI 2024-68-I.0 “Origami Reconfigurable Beam-steering Antennas with META-surfaces for Communication on Small Satellites - ORBIT-META” (CUP: F93C24000550001); HORIZON-TMA-MSCA-SE HORIZON TMA MSCA Staff Exchanges (101182995) “Cr4+:YAG/Polymer nanocomposite as alternative materials for Q-switched lasers: properties, modeling, and applications - ALTER-Q”

Data availability

Data will be made available on request.

References

[1] K. Ke, C. Xia, M.N. Islam, M.J. Welsh, M.J. Freeman, Mid-infrared absorption spectroscopy and differential damage in vitro between lipids and proteins by an all-fiber-integrated supercontinuum laser, Opt. Express 17 (2009) 12627, https://doi.org/10.1364/OE.17.012627.

[2] A.B. Seddon, M.C. Farries, J.J. Nunes, B. Xiao, D. Furniss, E. Barney, S. Phang, S. Chahal, N. Kalfagiannis, Ł. Sojka, S. Sujecki, Short review and prospective: chalcogenide glass mid-infrared fibre lasers, Eur. Phys. J. Plus 139 (2024) 142, https://doi.org/10.1140/epjp/s13360-023-04841-1.

[3] Z. Wang, B. Zhang, J. Liu, Y. Song, H. Zhang, Recent developments in mid-infrared fiber lasers: status and challenges, Opt. Laser Technol. 132 (2020) 106497, https://doi.org/10.1016/j.optlastec.2020.106497.

[4] G. Flores Rangel, L. Diaz De León Martínez, L.S. Walter, B. Mizaikoff, Recent advances and trends in mid-infrared chem/bio sensors, TrAC Trends Anal. Chem. 180 (2024) 117916, https://doi.org/10.1016/j.trac.2024.117916.

[5] J. Li, Y. Zhou, L. He, Z. Wang, W. Ma, Y. Ji, L. Song, Open-path sensor for atmospheric NO detection based on mid-infrared laser absorption spectroscopy, Infrared Phys. Technol. 133 (2023) 104813, https://doi.org/10.1016/j.infrared.2023.104813.

[6] R. Sur, W.Y. Peng, C. Strand, R. Mitchell Spearrin, J.B. Jeffries, R.K. Hanson, A. Bekal, P. Halder, S.P. Poonacha, S. Vartak, A.K. Sridharan, Mid-infrared laser absorption spectroscopy of NO2 at elevated temperatures, J. Quant. Spectrosc. Radiat. Transf. 187 (2017) 364–374, https://doi.org/10.1016/j.jqsrt.2016.10.016.

[7] S. Chandran, J. Orphal, A.A. Ruth, Experimental observation of the $\nu1+3\nu3$ combination bands of 16O14N18O and 18O14N18O in the near infrared spectral region, Heliyon 10 (2024) e24853, https://doi.org/10.1016/j.heliyon.2024.e24853.

[8] D.M. Sonnenfroh, M.G. Allen, W.T. Rawlins, C.F. Gmachl, F. Capasso, A. L. Hutchinson, D.L. Sivco, A.Y. Cho, in: T. Vo-Dinh, R.L. Spellicy (Eds.), Pollutant Emission Monitoring Using QC Laser-Based Mid-IR Sensors, 2001, p. 86, https://doi.org/10.1117/12.417364. Boston, MA.

[9] M.L. Van Gelder, M.E. Ressler, E.F. Van Dishoeck, P. Nazari, B. Tabone, J. H. Black, Ł. Tychoniec, L. Francis, M. Barsony, H. Beuther, A. Caratti O Garatti, Y. Chen, C. Gieser, V.J.M. Le Gouellec, P.J. Kavanagh, P.D. Klaassen, B.W.P. Lew, H. Linnartz, L. Majumdar, G. Perotti, W.R.M. Rocha, JOYS+: mid-infrared detection of gas-phase SO_2 emission in a low-mass protostar: the case of NGC 1333 IRAS 2A: hot core or accretion shock? Astron. Astrophys. 682 (2024) A78, https://doi.org/10.1051/0004-6361/202348118.

[10] R. Sa, L. Bu, Q. Wang, J. Zhou, Spectral characteristics of polluted gases and their detection by mid-infrared differential absorption lidar, Optik 149 (2017) 113–124, https://doi.org/10.1016/j.ijleo.2017.09.008.

[11] J. Li, S. Guo, Z. Wang, Y. Wei, W. Liu, Z. Xi, S. Yao, Measurement of NH3 emission in CH4/NH3 combustion exhaust gas with the mid-infrared laser absorption, Infrared Phys. Technol. 147 (2025) 105802, https://doi.org/10.1016/j.infrared.2025.105802.

[12] R.I. Woodward, M.R. Majewski, D.D. Hudson, S.D. Jackson, Swept-wavelength mid-infrared fiber laser for real-time ammonia gas sensing, APL Photonics 4 (2019) 020801, https://doi.org/10.1063/1.5065415.

[13] L. Qi, W. Chen, S. Qiao, J. Jiang, Y. Shi, Y. Ma, Mid-infrared quasi-distributed carbon monoxide gas sensing based on QEPAS and hollow waveguide, Infrared Phys. Technol. 145 (2025) 105653, https://doi.org/10.1016/j.infrared.2024.105653.

[14] F. Ottonello-Briano, C. Errando-Herranz, H. Rödjegård, H. Martin, H. Sohlström, K.B. Gylfason, Carbon dioxide absorption spectroscopy with a mid-infrared silicon photonic waveguide, Opt. Lett. 45 (2020) 109, https://doi.org/10.1364/OL.45.000109.

[15] B. Guo, Y. Wang, C. Peng, H.L. Zhang, G.P. Luo, H.Q. Le, C. Gmachl, D.L. Sivco, M.L. Peabody, A.Y. Cho, Laser-based mid-infrared reflectance imaging of biological tissues, Opt. Express 12 (2004) 208, https://doi.org/10.1364/OPEX.12.000208.

[16] A. Theodosiou, K. Kalli, O. Sapir-Henderson, Acetone gas sensing using a hybrid mid-infrared fluoride fiber laser, IEEE Sens. J. 24 (2024) 20669–20673, https://doi.org/10.1109/JSEN.2024.3400369.

[17] N. Alizadeh, H. Jamalabadi, F. Tavoli, Breath acetone sensors as non-invasive health monitoring systems: a review, IEEE Sens. J. 20 (2020) 5–31, https://doi.org/10.1109/JSEN.2019.2942693.

[18] A. Rydosz, Sensors for enhanced detection of acetone as a potential tool for noninvasive diabetes monitoring, Sensors 18 (2018) 2298, https://doi.org/10.3390/s18072298.

[19] C. Lourenço, C. Turner, Breath analysis in disease diagnosis: methodological considerations and applications, Metabolites 4 (2014) 465–498, https://doi.org/10.3390/metabo4020465.

[20] V.S. Serebryakov, É.V. Boĭko, A.G. Kalintsev, A.F. Kornev, A.S. Narivonchik, A. L. Pavlova, Mid-IR laser for high-precision surgery, J. Opt. Technol. 82 (2015) 781, https://doi.org/10.1364/JOT.82.000781.

[21] S.M. Cristescu, S.T. Persijn, S. Te Lintel Hekkert, F.J.M. Harren, Laser-based systems for trace gas detection in life sciences, Appl. Phys. B 92 (2008) 343, https://doi.org/10.1007/s00340-008-3127-y.

[22] A. Genner, P. Martín-Mateos, H. Moser, B. Lendl, A quantum cascade laser-based multi-gas sensor for ambient air monitoring, Sensors 20 (2020) 1850, https://doi.org/10.3390/s20071850.

[23] Z. Du, S. Zhang, J. Li, N. Gao, K. Tong, Mid-infrared tunable laser-based broadband fingerprint absorption spectroscopy for trace gas sensing: a review, Appl. Sci. 9 (2019) 338, https://doi.org/10.3390/app9020338.

[24] G. Wysocki, Y. Bakhirkin, S. So, F.K. Tittel, C.J. Hill, R.Q. Yang, M.P. Fraser, Dual interband cascade laser based trace-gas sensor for environmental monitoring, Appl. Opt. 46 (2007) 8202, https://doi.org/10.1364/AO.46.008202.

[25] L. Melchiorre, F. Anelli, G. Menduni, A. Annunziato, L. Bodin, S. Cozic, G. Magno, A. Sampaolo, F. Prudenzano, V. Spagnolo, Dual-gas quartz-enhanced photoacoustic spectroscopy sensor exploiting two fiber-combined interband

cascade lasers, Photoacoustics 42 (2025) 100689, https://doi.org/10.1016/j.pacs.2025.100689.
[26] D. Huang, E.A. Swanson, C.P. Lin, J.S. Schuman, W.G. Stinson, W. Chang, M. R. Hee, T. Flotte, K. Gregory, C.A. Puliafito, J.G. Fujimoto, Optical coherence tomography, Science 254 (1991) 1178–1181, https://doi.org/10.1126/science.1957169.
[27] A. Gunalan, L.S. Mattos, Towards OCT-guided endoscopic laser surgery—a review, Diagnostics 13 (2023) 677, https://doi.org/10.3390/diagnostics13040677.
[28] N.M. Israelsen, C.R. Petersen, A. Barh, D. Jain, M. Jensen, G. Hannesschläger, P. Tidemand-Lichtenberg, C. Pedersen, A. Podoleanu, O. Bang, Real-time high-resolution mid-infrared optical coherence tomography, Light Sci. Appl. 8 (2019) 11, https://doi.org/10.1038/s41377-019-0122-5.
[29] S. Aumann, S. Donner, J. Fischer, F. Müller, Optical coherence tomography (OCT): principle and technical realization, in: J.F. Bille (Ed.), High Resolut. Imaging Microsc. Ophthalmol., Springer International Publishing, Cham, 2019, pp. 59–85, https://doi.org/10.1007/978-3-030-16638-0_3.
[30] S.R. Chinn, E.A. Swanson, J.G. Fujimoto, Optical coherence tomography using a frequency-tunable optical source, Opt. Lett. 22 (1997) 340, https://doi.org/10.1364/OL.22.000340.
[31] A.F. Fercher, C.K. Hitzenberger, G. Kamp, S.Y. El-Zaiat, Measurement of intraocular distances by backscattering spectral interferometry, Opt. Commun. 117 (1995) 43–48, https://doi.org/10.1016/0030-4018(95)00119-S.
[32] E. Götzinger, M. Pircher, B. Baumann, C. Hirn, C. Vass, C.K. Hitzenberger, Analysis of the origin of atypical scanning laser polarimetry patterns by polarization-sensitive optical coherence tomography, Investig. Opthalmology Vis. Sci. 49 (2008) 5366, https://doi.org/10.1167/iovs.08-2081.
[33] Y. Liang, X. Wang, Z. Gu, Y. Guan, L. He, K. Xia, X. Wang, S. Dai, X. Shen, Z. Liu, High extinction-ratio and near-zero dispersion chalcogenide polarization maintaining photonic crystal fibers in mid-infrared, J. Light. Technol. 42 (2024) 5691–5697, https://doi.org/10.1109/JLT.2024.3399162.
[34] T. Xu, M. Zhong, X. Liang, J. Liu, B. Yan, J. Xiao, K. Jiao, X. Wang, N. Si, Z. Pan, Z. Zhao, X. Wang, P. Zhang, Q. Nie, S. Bai, R. Wang, J. Zhang, High extinction-ratio microstructure fiber based on chalcogenide glasses, J. Am. Ceram. Soc. 104 (2021) 5671–5678, https://doi.org/10.1111/jace.17936.
[35] H.T. Tong, A. Koumura, A. Nakatani, H.P.T. Nguyen, M. Matsumoto, G. Sakai, T. Suzuki, Y. Ohishi, Chalcogenide all-solid hybrid microstructured optical fiber with polarization maintaining properties and its mid-infrared supercontinuum generation, Opt. Express 30 (2022) 25433, https://doi.org/10.1364/OE.459745.
[36] Y. Li, X. He, Z. Wen, M. Wu, G. Tang, X. Song, Q. Qian, Research progress on 2 μm germanate glass fibers and their laser applications, Ceram. Int. 51 (2025) 16584–16592, https://doi.org/10.1016/j.ceramint.2024.12.076.
[37] H. Ren, L. Shen, A.F.J. Runge, T.W. Hawkins, J. Ballato, U. Gibson, A.C. Peacock, Low-loss silicon core fibre platform for mid-infrared nonlinear photonics, Light Sci. Appl. 8 (2019) 105, https://doi.org/10.1038/s41377-019-0217-z.
[38] M. Poulain, M. Poulain, J. Lucas, Verres fluores au tetrafluorure de zirconium proprietes optiques d'un verre dope au Nd3+, Mater. Res. Bull. 10 (1975) 243–246, https://doi.org/10.1016/0025-5408(75)90106-3.
[39] K. Grebnev, B. Perminov, T.T. Fernandez, A. Fuerbach, M. Chernysheva, Fluoride and chalcogenide glass fiber components for mid-infrared lasers and amplifiers: breakthroughs, challenges, and future perspective, APL Photonics 9 (2024) 110901, https://doi.org/10.1063/5.0225887.
[40] G. Tao, H. Ebendorff-Heidepriem, A.M. Stolyarov, S. Danto, J.V. Badding, Y. Fink, J. Ballato, A.F. Abouraddy, Infrared fibers, Adv. Opt. Photonics 7 (2015) 379, https://doi.org/10.1364/AOP.7.000379.
[41] M.F. Churbanov, I.V. Skripachev, G.E. Snopatin, L.A. Ketkova, V.G. Plotnichenko, The problems of optical loss reduction in arsenic sulfide glass IR fibers, Opt. Mater. 102 (2020) 109812, https://doi.org/10.1016/j.optmat.2020.109812.
[42] F.B. Slimen, S. Chen, J. Lousteau, Y. Jung, N. White, S. Alam, D.J. Richardson, F. Poletti, Highly efficient -Tm^{3+} doped germanate large mode area single mode fiber laser, Opt. Mater. Express 9 (2019) 4115, https://doi.org/10.1364/OME.9.004115.
[43] Y.O. Aydin, F. Maes, V. Fortin, S.T. Bah, R. Vallée, M. Bernier, Endcapping of high-power 3 μm fiber lasers, Opt. Express 27 (2019) 20659, https://doi.org/10.1364/OE.27.020659.
[44] Y. Lu, M. Cai, R. Cao, S. Qian, S. Xu, J. Zhang, Er 3+ doped germanate–tellurite glass for mid-infrared 2.7 μm fiber laser material, J. Quant. Spectrosc. Radiat. Transf. 171 (2016) 73–81, https://doi.org/10.1016/j.jqsrt.2015.12.014.
[45] J. Li, H. Yang, Z. Lun, Z. Wen, J. Lu, G. Tang, M. Wu, X. Song, Q. Qian, Accelerated design of Tm3+-doped multicomponent germanate laser glasses via neighboring glassy compounds model, Mater. Des. 254 (2025) 114133, https://doi.org/10.1016/j.matdes.2025.114133.
[46] X. Wen, G. Tang, Q. Yang, X. Chen, Q. Qian, Q. Zhang, Z. Yang, Highly Tm3+ doped germanate glass and its single mode fiber for 2.0 μm laser, Sci. Rep. 6 (2016) 20344, https://doi.org/10.1038/srep20344.
[47] B. Gleason, K. Richardson, L. Sisken, C. Smith, Refractive index and thermo-optic coefficients of Ge-as-Se chalcogenide glasses, Int. J. Appl. Glass Sci. 7 (2016) 374–383, https://doi.org/10.1111/ijag.12190.
[48] B. Hauke, E.R. Barney, E. Pakhomenko, M. Jesuit, M. Packard, A. Crego, G. Tarantino, M. Affatigato, S. Feller, Structure and glass transition temperatures of tellurite glasses, Phys. Chem. Glas. Eur. J. Glass Sci. Technol. Part B 61 (2020) 21–26, https://doi.org/10.13036/17533562.61.1.11.
[49] L. Kadathala, J.-H. In, J. Park, J. Choi, Thermal and mechanical properties of tellurite glasses for mid-IR molded glass lens applications, in: R. Rascher, R. Williamson, D.W. Kim (Eds.), Opt. Manuf. Test. XII, SPIE, San Diego, United States, 2018, p. 63, https://doi.org/10.1117/12.2320438.
[50] A.V. Andrianov, M.P. Marisova, E.A. Anashkina, Thermo-optical sensitivity of whispering gallery modes in As2S3 chalcogenide glass microresonators, Sensors 22 (2022) 4636, https://doi.org/10.3390/s22124636.
[51] F. Anelli, A. Annunziato, A.M. Loconsole, V.V. Francione, S. Cozic, S. Poulain, F. Prudenzano, Mid-infrared interferometry with non-adiabatic tapered ZBLAN optical fiber, Opt. Express 32 (2024) 18944, https://doi.org/10.1364/OE.521239.
[52] H. Li, J. Lousteau, W.N. MacPherson, X. Jiang, H.T. Bookey, J.S. Barton, A. Jha, A.K. Kar, Thermal sensitivity of tellurite and germanate optical fibers, Opt. Express 15 (2007) 8857, https://doi.org/10.1364/OE.15.008857.
[53] F. Anelli, A. Annunziato, A.M. Loconsole, V.V. Francione, S. Cozic, S. Poulain, F. Prudenzano, A temperature sensor based on all-fiber mach-zender interferometer with indium fluoride glass, in: S. Taccheo, M.R. Cicconi, M. L. Jäger (Eds.), Fiber Lasers Glass Photonics Mater. Appl. IV, SPIE, Strasbourg, France, 2024, p. 39, https://doi.org/10.1117/12.3017496.
[54] M. Khalid, M. Usman, I. Arshad, Germanate glass for laser applications in ~ 2.1 μm spectral region: a review, Heliyon 9 (2023) e13031, https://doi.org/10.1016/j.heliyon.2023.e13031.
[55] T. Cheng, X. Chen, Y. Gao, F. Zhang, B. Li, X. Yan, X. Zhang, F. Wang, T. Suzuki, Y. Ohishi, Single-mode tellurite optical fiber for temperature measurement based on the self-phase modulation effect, Opt. Lett. 47 (2022) 874, https://doi.org/10.1364/OL.449945.
[56] M. Rezvani, A. Yousefi Dizaj, A. Rahimian, T. Joudi, The effect of Er on optical and mechanical properties of As2S3 glasses quenched in different media, Eur. Phys. J. Plus 135 (2020) 532, https://doi.org/10.1140/epjp/s13360-020-00502-9.
[57] O. Henderson-Sapir, D.J. Ottaway, A decade of mid-infrared, 3.5 μ m dual-wavelength pumped fiber lasers, review and perspective, APL Photonics 9 (2024) 100901, https://doi.org/10.1063/5.0232437.
[58] G. Woyessa, K. Kwarkye, M.K. Dasa, C.R. Petersen, R. Sidharthan, S. Chen, S. Yoo, O. Bang, Power stable 1.5–10.5 μm cascaded mid-infrared supercontinuum laser without thulium amplifier, Opt. Lett. 46 (2021) 1129, https://doi.org/10.1364/OL.416123.
[59] S. Venck, F. St-Hilaire, L. Brilland, A.N. Ghosh, R. Chahal, C. Caillaud, M. Meneghetti, J. Troles, F. Joulain, S. Cozic, S. Poulain, G. Huss, M. Rochette, J. M. Dudley, T. Sylvestre, 2–10 μm mid-infrared fiber-based supercontinuum laser source: experiment and simulation, Laser Photonics Rev. 14 (2020) 2000011, https://doi.org/10.1002/lpor.202000011.
[60] K. Guo, R.A. Martinez, G. Plant, L. Maksymiuk, B. Janiszewski, M.J. Freeman, R. L. Maynard, M.N. Islam, F.L. Terry, R. Bedford, R. Gibson, F. Chenard, S. Chatigny, A.I. Ifarraguerri, Generation of near-diffraction-limited, high-power supercontinuum from 157 μm to 12 μm with cascaded fluoride and chalcogenide fibers, Appl. Opt. 57 (2018) 2519, https://doi.org/10.1364/AO.57.002519.
[61] M.H.M. Shamim, I. Alamgir, W. Correr, Y. Messaddeq, M. Rochette, Soliton self-frequency shift in a cascade of silica, fluoride, and chalcogenide fibers, J. Light. Technol. 42 (2024) 6063–6069, https://doi.org/10.1109/JLT.2024.3407069.
[62] A.V. Gladyshev, D.S. Dubrovskii, A.F. Kosolapov, I.V. Morozov, A.I. Boltalin, I. A. Bufetov, Mid-infrared lasers and supercontinuum sources based on stimulated Raman scattering in gas-filled hollow-core fibers, IEEE J. Sel. Top. Quantum Electron. 30 (2024) 1–7, https://doi.org/10.1109/JSTQE.2024.3385374.
[63] A.A. Krylov, A.V. Gladyshev, A.K. Senatorov, A.N. Kolyadin, A.F. Kosolapov, M. M. Khudyakov, M.E. Likhachev, I.A. Bufetov, 1.56-to-2.84 μm SRS conversion of chirped pulses of a high-power erbium fibre laser in a methane-filled hollow-core revolver fibre, Quantum Electron 52 (2022) 274–277, https://doi.org/10.1070/QEL18003.
[64] A.I. Adamu, Y. Wang, MdS. Habib, ManojK. Dasa, J.E. Antonio-Lopez, R. Amezcua-Correa, O. Bang, C. Markos, Multi-wavelength high-energy gas-filled fiber Raman laser spanning from 1.53 μm to 2.4 μm, Opt. Lett. 46 (2021) 452, https://doi.org/10.1364/OL.411003.
[65] Y. Wang, M.K. Dasa, A.I. Adamu, J.E. Antonio-Lopez, MdS. Habib, R. Amezcua-Correa, O. Bang, C. Markos, High pulse energy and quantum efficiency mid-infrared gas Raman fiber laser targeting CO_2 absorption at 4.2 μm, Opt. Lett. 45 (2020) 1938, https://doi.org/10.1364/OL.389613.
[66] A.V. Gladyshev, I.A. Bufetov, E.M. Dianov, A.F. Kosolapov, M.M. Khudyakov, Y. P. Yatsenko, A.N. Kolyadin, A.A. Krylov, A.D. Pryamikov, A.S. Biriukov, M. E. Likhachev, 2.9, 3.3, and 3.5 μm Raman lasers based on revolver hollow-core silica fiber filled by 1H2/D2 gas mixture, IEEE J. Sel. Top. Quantum Electron 24 (2018) 1–8, https://doi.org/10.1109/JSTQE.2018.2810378.
[67] W. Huang, Y. Cui, Z. Li, Z. Zhou, Y. Chen, Z. Wang, Diode-pumped single-pass tunable mid-infrared gas Raman source by methane-filled hollow-core fiber, Laser Phys. Lett. 16 (2019) 085107, https://doi.org/10.1088/1612-202X/ab2a78.
[68] W. Huang, Z. Wang, Z. Zhou, W. Pei, Y. Cui, X. Li, Z. Li, J. Chen, Tunable fiber gas Raman laser of 6 W at 2.9 μm by deuterium-filled hollow-core fiber, IEEE J. Sel. Top. Quantum Electron. 30 (2024) 1–7, https://doi.org/10.1109/JSTQE.2023.3292594.
[69] X. Zhu, D. Zhao, B. Zhang, L. Yang, J. Yao, Y. Yang, S. Liu, J. Hou, Spectrally flat mid-infrared supercontinuum pumped by a high power 2 μm noise-like pulse, Opt. Express 31 (2023) 13182, https://doi.org/10.1364/OE.487291.
[70] K. Xie, H. Lei, X. Wang, X. Zhao, S. Wang, H. Luo, J. Li, High-power flat supercontinuum generation by using UHNA7 fiber with spectrum of 1.77-3.31 μ m, IEEE Photonics Technol. Lett. 36 (2024) 405–408, https://doi.org/10.1109/LPT.2024.3359651.
[71] H. Lei, X. Wang, Z. Li, K. Xie, X. Zhou, H. Luo, Z. Luo, J. Li, All-fiber ultra-flat supercontinuum source covering 1.85–3.57 μm based on germania-core fiber, Opt. Laser Technol. 164 (2023) 109478, https://doi.org/10.1016/j.optlastec.2023.109478.

[72] M.A. Abbas, K.E. Jahromi, M. Nematollahi, R. Krebbers, N. Liu, G. Woyessa, O. Bang, L. Huot, F.J.M. Harren, A. Khodabakhsh, Fourier transform spectrometer based on high-repetition-rate mid-infrared supercontinuum sources for trace gas detection, Opt. Express 29 (2021) 22315, https://doi.org/10.1364/OE.425995.
[73] L. Yang, B. Zhang, X. He, K. Deng, S. Liu, J. Hou, High-power mid-infrared supercontinuum generation in a fluoroindate fiber with over 2 W power beyond 3.8 μm, Opt. Express 28 (2020) 14973, https://doi.org/10.1364/OE.393132.
[74] J. Zeng, A.E. Akosman, M.Y. Sander, Supercontinuum generation from a thulium ultrafast fiber laser in a high NA silica fiber, IEEE Photonics Technol. Lett. 31 (2019) 1787–1790, https://doi.org/10.1109/LPT.2019.2946835.
[75] L. Yang, B. Zhang, X. He, K. Deng, S. Liu, J. Hou, 20.6 W mid-infrared supercontinuum generation in ZBLAN fiber with spectrum of 1.9–4.3 μm, J. Light. Technol. 38 (2020) 5122–5127, https://doi.org/10.1109/JLT.2020.2999730.
[76] U. Møller, Y. Yu, C.R. Petersen, I. Kubat, L. Brilland, D. Méchin, J. Troles, B. Luther-Davies, O. Bang, High average power mid-infrared supercontinuum generation in a suspended core chalcogenide fiber, in: Adv. Photonics, OSA, Barcelona, 2014, https://doi.org/10.1364/BGPP.2014.JM5A.54 p. JM5A.54.
[77] A. Fürbach, T.T. Ha, T.T. Fernandez, All-fiber mid-infrared laser sources, in: S. Taccheo, M.R. Cicconi, M.L. Jäger (Eds.), Fiber Lasers Glass Photonics Mater, vol. IV, Appl., SPIE, Strasbourg, France, 2024, p. 25, https://doi.org/10.1117/12.3024839.
[78] S.D. Jackson, R.K. Jain, Fiber-based sources of coherent MIR radiation: key advances and future prospects (invited), Opt. Express 28 (2020) 30964, https://doi.org/10.1364/OE.400003.
[79] X. Liang, M. Zhong, T. Xu, J. Xiao, K. Jiao, X. Wang, Y. Bin, J. Liu, X. Wang, Z. Zhao, S. Bai, S. Li, D. Du, Y. He, Q. Nie, R. Wang, Mid-infrared single-mode Ge-as-S fiber for high power laser delivery, J. Light. Technol. 40 (2022) 2151–2156, https://doi.org/10.1109/JLT.2021.3130182.
[80] F. Jobin, P. Paradis, Y.O. Aydin, T. Boilard, V. Fortin, J.-C. Gauthier, M. Lemieux-Tanguay, S. Magnan-Saucier, L.-C. Michaud, S. Mondor, L.-P. Pleau, L. Talbot, M. Bernier, R. Vallée, Recent developments in lanthanide-doped mid-infrared fluoride fiber lasers [Invited], Opt. Express 30 (2022) 8615, https://doi.org/10.1364/OE.450929.
[81] A. Tyazhev, F. Starecki, S. Cozic, P. Loiko, L. Guillemot, A. Braud, F. Joulain, M. Tang, T. Godin, A. Hideur, P. Camy, Watt-level efficient 2.3 μm thulium fluoride fiber laser, Opt. Lett. 45 (2020) 5788, https://doi.org/10.1364/OL.403450.
[82] S.D. Jackson, M. Pollnau, Jianfeng Li, diode pumped erbium cascade fiber lasers, IEEE J. Quantum Electron. 47 (2011) 471–478, https://doi.org/10.1109/JQE.2010.2091256.
[83] J. Zhang, R. Wang, S. Fu, Q. Sheng, W. Xia, L. Zhang, W. Shi, J. Yao, Erbium-doped ZBLAN fiber laser pumped at 1.7 μm for emission at 2.8 μm, Opt. Lett. 47 (2022) 3684, https://doi.org/10.1364/OL.463186.
[84] C. Guo, P. Shen, S. Ruan, J. Wang, Q. Lue, Dual-wavelength pumped 2.8 μm Er-doped ZBLAN fiber laser with high overall optical efficiency, Infrared Phys. Technol. 132 (2023) 104739, https://doi.org/10.1016/j.infrared.2023.104739.
[85] J. Zhang, Q. Sheng, S. Fu, Z. Zhou, L. Zhang, W. Shi, J. Yao, Efficient 2.8-μm Er-doped all-fiber laser based on a low optical feedback cavity, Opt. Express 33 (2025) 9091, https://doi.org/10.1364/OE.553867.
[86] V. Fortin, M. Bernier, S.T. Bah, R. Vallée, 30 W fluoride glass all-fiber laser at 294 μm, Opt. Lett. 40 (2015) 2882, https://doi.org/10.1364/OL.40.002882.
[87] S. Wang, J. Zhang, N. Xu, S. Jia, G. Brambilla, P. Wang, 2.9 μm lasing from a Ho^{3+}/Pr^{3+} co-doped AlF_3 -based glass fiber pumped by a 1150 nm laser, Opt. Lett. 45 (2020) 1216, https://doi.org/10.1364/OL.384216.
[88] Z. Cheng, Z. Zhang, C. Xu, Y. Dong, S. Wang, C. Guan, S. Jia, P. Wang, Highly efficient 2.86 μm laser in Ho3+-doped fluoroindate fiber via dual-wavelength pumping, Opt. Laser Technol. 183 (2025) 112346, https://doi.org/10.1016/j.optlastec.2024.112346.
[89] M.R. Majewski, R.I. Woodward, S.D. Jackson, Dysprosium-doped ZBLAN fiber laser tunable from 28 μm to 34 μm, pumped at 17 μm, Opt. Lett. 43 (2018) 971, https://doi.org/10.1364/OL.43.000971.
[90] V. Fortin, F. Jobin, M. Larose, M. Bernier, R. Vallée, 10-W-level monolithic dysprosium-doped fiber laser at 324 μm, Opt. Lett. 44 (2019) 491, https://doi.org/10.1364/OL.44.000491.
[91] R.I. Woodward, M.R. Majewski, G. Bharathan, D.D. Hudson, A. Fuerbach, S. D. Jackson, Watt-level dysprosium fiber laser at 315 μm with 73% slope efficiency, Opt. Lett. 43 (2018) 1471, https://doi.org/10.1364/OL.43.001471.
[92] M.C. Falconi, A.M. Loconsole, A. Annunziato, S. Cozic, S. Poulain, F. Prudenzano, Design of a broadband erbium-doped fluoroindate fiber laser emitting up to 3.91 μm, J. Light. Technol. 41 (2023) 6065–6072, https://doi.org/10.1109/JLT.2023.3275168.
[93] S. Duval, J.-C. Gauthier, L.-R. Robichaud, P. Paradis, M. Olivier, V. Fortin, M. Bernier, M. Piché, R. Vallée, Watt-level fiber-based femtosecond laser source tunable from 28 to 36 μm, Opt. Lett. 41 (2016) 5294, https://doi.org/10.1364/OL.41.005294.
[94] V. Fortin, F. Maes, M. Bernier, S.T. Bah, M. D'Auteuil, R. Vallée, Watt-level erbium-doped all-fiber laser at 344 μm, Opt. Lett. 41 (2016) 559, https://doi.org/10.1364/OL.41.000559.
[95] O. Henderson-Sapir, A. Malouf, N. Bawden, J. Munch, S.D. Jackson, D.J. Ottaway, Recent advances in 3.5 μ m erbium-doped mid-infrared fiber lasers, IEEE J. Sel. Top. Quantum Electron. 23 (2017) 6–14, https://doi.org/10.1109/JSTQE.2016.2615961.
[96] L. Zhang, S. Fu, Q. Sheng, X. Luo, J. Zhang, W. Shi, J. Yao, Widely tunable single-frequency Er-doped ZBLAN fiber laser with emission from 3.37 to 3.72 μm, Opt. Lett. 48 (2023) 6200, https://doi.org/10.1364/OL.505803.
[97] D.S. Lipatov, A.S. Lobanov, A.N. Guryanov, A.A. Umnikov, A.N. Abramov, M. M. Khudyakov, M.E. Likhachev, O.G. Morozov, Fabrication and characterization of Er/Yb Co-doped fluorophosphosilicate glass core optical fibers, Fibers 9 (2021) 15, https://doi.org/10.3390/fib9030015.
[98] Y. Chu, J. Ren, J. Zhang, G. Peng, J. Yang, P. Wang, L. Yuan, Ce3+/Yb3+/Er3+ triply doped bismuth borosilicate glass: a potential fiber material for broadband near-infrared fiber amplifiers, Sci. Rep. 6 (2016) 33865, https://doi.org/10.1038/srep33865.
[99] L. Sojka, Z. Tang, D. Jayasuriya, M. Shen, D. Furniss, E. Barney, T.M. Benson, A. B. Seddon, S. Sujecki, Ultra-broadband mid-infrared emission from a Pr^{3+}/Dy^{3+} co-doped selenide-chalcogenide glass fiber spectrally shaped by varying the pumping arrangement [Invited], Opt. Mater. Express 9 (2019) 2291, https://doi.org/10.1364/OME.9.002291.
[100] N. Xu, P. Wang, S. Wang, M. Liu, J. Wang, Z. Li, Z. Yang, Wavelength extension beyond 3 μm in a Ho^{3+}/Pr^{3+} co-doped AlF_3 -based fiber laser, Opt. Lett. 49 (2024) 2113, https://doi.org/10.1364/OL.520761.
[101] T. Boilard, V. Fortin, M. Lemieux-Tanguay, P. Paradis, P. Du Teilleul, J.-Y. Carrée, R. Vallée, M. Bernier, 1.7 W holmium-doped fluoroindate fiber laser at 3920 nm, Opt. Lett. 49 (2024) 2677, https://doi.org/10.1364/OL.522233.
[102] A.M. Loconsole, M.C. Falconi, V. Portosi, F. Prudenzano, Numerical design of a gain-switched pulsed laser at 3.92 μm wavelength based on a Ho^{3+} -doped fluoroindate fiber, J. Light. Technol. 39 (2021) 3276–3283, https://doi.org/10.1109/JLT.2021.3064764.
[103] F. Zhou, J. Li, H. Luo, F. Quellette, Y. Liu, Numerical analysis of 3.92 μm dual-wavelength pumped heavily-holmium-doped fluoroindate fiber lasers, J. Light. Technol. 39 (2021) 633–645, https://doi.org/10.1109/JLT.2020.3033335.
[104] Z. Cheng, Z. Zhang, R. Wang, S. Wang, X. Li, S.N. Chormaic, S. Jia, P. Wang, Numerical modeling of dual-wavelength pumped heavily-Ho^{3+} -doped fluoroindate fiber lasers with efficient output at 3.92 μm, J. Light. Technol. 41 (2023) 7021–7028, https://doi.org/10.1109/JLT.2023.3295126.
[105] A.M. Loconsole, M.C. Falconi, A. Annunziato, S. Cozic, S. Poulain, F. Prudenzano, Design of a mid-IR laser based on a Ho:Nd-codoped fluoroindate fiber, J. Light. Technol. 41 (2023) 702–708, https://doi.org/10.1109/JLT.2022.3218190.
[106] Z. Wu, J. Cao, W. Liu, C. Shang, Z. Fan, H. Yue, C. Wei, Y. Liu, Theoretical study on cascade energy-transfer pumping heavily holmium-doped fluoroindate fiber laser at ∼ 4 μm with high-efficiency, Opt. Laser Technol. 181 (2025) 111939, https://doi.org/10.1016/j.optlastec.2024.111939.
[107] A.M. Loconsole, V.V. Francione, A. Annunziato, F. Anelli, F. Prudenzano, Design of a high performance mid-IR fiber laser based on Pr^{3+} -doped fluoroindate glass, J. Light. Technol. 42 (2024) 2488–2493, https://doi.org/10.1109/JLT.2023.3338139.
[108] M.R. Majewski, R.I. Woodward, J.-Y. Carreé, S. Poulain, M. Poulain, S.D. Jackson, Emission beyond 4 μm and mid-infrared lasing in a dysprosium-doped indium fluoride (InF_3) fiber, Opt. Lett. 43 (2018) 1926, https://doi.org/10.1364/OL.43.001926.
[109] M.R. Majewski, S.D. Jackson, Numerical design of $4\,\mu {\rm m}$-class dysprosium fluoride fiber lasers, J. Light. Technol. 39 (2021) 5103–5110, https://doi.org/10.1109/JLT.2021.3080296.
[110] Y. Zhou, A. Yang, G. Yang, Q. Qiu, X. Zhang, Z. Zhang, Y. Xing, J. Peng, H. Li, Y. Chu, J. Li, N. Dai, 3 × 1 fiber signal combiner with high beam quality Gaussian-like beam for a 10kW-level fiber laser, Opt. Express 31 (2023) 2780, https://doi.org/10.1364/OE.475281.
[111] É. Ducharme, S. Virally, R.I. Becerra-Deana, C. Boudoux, N. Godbout, Viscosity of fluoride glass fibers for fused component fabrication, Appl. Opt. 61 (2022) 5031, https://doi.org/10.1364/AO.455528.
[112] T. Uthayakumar, R. Vasantha Jayakantha Raja, All-optical photonic crystal fiber couplers, in: Encycl. Mater. Electron., Elsevier, 2023, pp. 260–279, https://doi.org/10.1016/B978-0-12-819728-8.00017-6.
[113] V.D. Fedorov, V.V. Sakharov, A.M. Provorova, P.B. Baskov, M.F. Churbanov, V. S. Shiryaev, M. Poulain, M. Poulain, A. Boutarfaia, Kinetics of isothermal crystallization of fluoride glasses, J. Non-Cryst. Solids 284 (2001) 79–84, https://doi.org/10.1016/S0022-3093(01)00383-0.
[114] A. Annunziato, F. Anelli, P.L.P. Du Teilleul, S. Cozic, S. Poulain, F. Prudenzano, Fused optical fiber combiner based on indium fluoride glass: perspectives for mid-IR applications, Opt. Express 30 (2022) 44160, https://doi.org/10.1364/OE.471090.
[115] S. Cozic, S. Boivinet, C. Pierre, J. Boulet, S. Poulain, M. Poulain, Splicing fluoride glass and silica optical fibers, EPJ Web Conf. 215 (2019) 04003, https://doi.org/10.1051/epjconf/201921504003.
[116] R. Al-Mahrous, R. Caspary, W. Kowalsky, A thermal splicing method to join silica and fluoride fibers, J. Light. Technol. 32 (2014) 303–308, https://doi.org/10.1109/JLT.2013.2290803.
[117] A. Theodosiou, O. Henderson-Sapir, Y. Baravets, O.T. Cobcroft, S.M. Sentschuk, J. A. Stone, D.J. Ottaway, P. Peterka, Understanding the temperature conditions for controlled splicing between silica and fluoride fibers, Adv. Photonics Res. 6 (2025) 2400150, https://doi.org/10.1002/adpr.202400150.
[118] X. Luo, Y. Tang, S. Ma, F. Dong, J. Wang, D. Ouyang, X. Liu, P. Yan, J. Wang, Q. Lue, S. Ruan, C. Guo, End-pump silica-fluoride fiber combiner utilizing tapering and assembling technique for mid-infrared laser systems, Infrared Phys. Technol. 145 (2025) 105645, https://doi.org/10.1016/j.infrared.2024.105645.
[119] S. Magnan-Saucier, S. Duval, C. Matte-Breton, Y.O. Aydin, V. Fortin, S. LaRochelle, M. Bernier, R. Vallée, Fuseless side-pump combiner for efficient fluoride-based double-clad fiber pumping, Opt. Lett. 45 (2020) 5828, https://doi.org/10.1364/OL.409174.

[120] B. Perminov, K. Grebnev, U. Hübner, M. Chernysheva, Side-polished silica-fluoride multimode fibre pump combiner for Mid-IR fibre lasers and amplifiers, Light Adv. Manuf. 5 (2024) 1, https://doi.org/10.37188/lam.2024.039.
[121] A. Séguin, R.I. Becerra-Deana, S. Virally, C. Boudoux, N. Godbout, Fabrication and characterization of indium fluoride multimode fused fiber couplers for the mid-infrared, Opt. Express 31 (2023) 33670, https://doi.org/10.1364/OE.501849.
[122] M. Rezaei, G.T. Zeweldi, M.H.M. Shamim, M. Rochette, Single-mode optical fiber couplers made of fluoride glass, Opt. Express 31 (2023) 27183, https://doi.org/10.1364/OE.495464.
[123] F. Anelli, A. Annunziato, A.M. Loconsole, V. Portosi, S. Cozic, P.L.P. Du Teilleul, S. Venck, S. Poulain, F. Prudenzano, Low-loss fluoride optical fiber coupler for mid-infrared applications, J. Light. Technol. 42 (2024) 2457–2463, https://doi.org/10.1109/JLT.2023.3337603.
[124] G.T. Zeweldi, N. Karampour, M. Rochette, Polarization-dependent fluoride fiber coupler and application to pulsed laser triggering, Opt. Lett. 50 (2025) 1365, https://doi.org/10.1364/OL.553776.
[125] H. Wang, T. Fujisawa, T. Sato, T. Mori, T. Sakamoto, Y. Yamashita, R. Imada, K. Nakajima, K. Saitoh, 6-mode and 10-mode photonic lantern mode multi/demultiplexers based on silica planar lightwave circuit, Opt. Commun. 529 (2023) 129098, https://doi.org/10.1016/j.optcom.2022.129098.
[126] T.A. Birks, I. Gris-Sánchez, S. Yerolatsitis, S.G. Leon-Saval, R.R. Thomson, The photonic lantern, Adv. Opt. Photonics 7 (2015) 107, https://doi.org/10.1364/AOP.7.000107.
[127] S.G. Leon-Saval, N.K. Fontaine, R. Amezcua-Correa, Photonic lantern as mode multiplexer for multimode optical communications, Opt. Fiber Technol. 35 (2017) 46–55, https://doi.org/10.1016/j.yofte.2016.08.005.
[128] F. Anelli, A. Annunziato, A.M. Loconsole, S. Venck, S. Cozic, F. Prudenzano, Mode-group selective photonic lantern based on indium fluoride optical fibers for mid-infrared, J. Light. Technol. 43 (2025) 280–287, https://doi.org/10.1109/JLT.2024.3450115.
[129] F. Anelli, S. Cozic, R. Weih, F. Prudenzano, Efficient mid-infrared light coupling into a single-mode optical fiber, Opt. Express (2025), https://doi.org/10.1364/OE.562190.
[130] S.J. Mihailov, C.W. Smelser, P. Lu, R.B. Walker, D. Grobnic, H. Ding, G. Henderson, J. Unruh, Fiber Bragg gratings made with a phase mask and 800-nm femtosecond radiation, Opt. Lett. 28 (2003) 995, https://doi.org/10.1364/OL.28.000995.
[131] S. Gross, M. Dubov, M.J. Withford, On the use of the Type I and II scheme for classifying ultrafast laser direct-write photonics, Opt. Express 23 (2015) 7767, https://doi.org/10.1364/OE.23.007767.
[132] R.J. Williams, R.G. Krämer, S. Nolte, M.J. Withford, Femtosecond direct-writing of low-loss fiber Bragg gratings using a continuous core-scanning technique, Opt. Lett. 38 (2013) 1918, https://doi.org/10.1364/OL.38.001918.
[133] S. Antipov, M. Ams, R.J. Williams, E. Magi, M.J. Withford, A. Fuerbach, Direct infrared femtosecond laser inscription of chirped fiber Bragg gratings, Opt. Express 24 (2016) 30, https://doi.org/10.1364/OE.24.000030.
[134] H. Poignant, S. Boj, E. Delevaque, M. Monerie, T. Taunay, P. Niay, P. Bernage, W. X. Xie, Efficiency and thermal behaviour of cerium-dopedfluorozirconate glassfibre Bragg gratings, Electron. Lett. 30 (1994) 1339–1341, https://doi.org/10.1049/el:19940886.
[135] M. Bernier, D. Faucher, R. Vallée, A. Saliminia, G. Androz, Y. Sheng, S.L. Chin, Bragg gratings photoinduced in ZBLAN fibers by femtosecond pulses at 800 nm, Opt. Lett. 32 (2007) 454, https://doi.org/10.1364/OL.32.000454.
[136] M. Bernier, D. Faucher, N. Caron, R. Vallée, Highly stable and efficient erbium-doped 28 μm all fiber laser, Opt. Express 17 (2009) 16941, https://doi.org/10.1364/OE.17.016941.
[137] D.D. Hudson, R.J. Williams, M.J. Withford, S.D. Jackson, Single-frequency fiber laser operating at 29 μm, Opt. Lett. 38 (2013) 2388, https://doi.org/10.1364/OL.38.002388.
[138] G. Bharathan, R.I. Woodward, M. Ams, D.D. Hudson, S.D. Jackson, A. Fuerbach, Direct inscription of Bragg gratings into coated fluoride fibers for widely tunable and robust mid-infrared lasers, Opt. Express 25 (2017) 30013, https://doi.org/10.1364/OE.25.030013.
[139] I. Chiamenti, T. Elsmann, A. Reupert, O. Kara, M. Becker, L. Wondraczek, M. Chernysheva, First-order fiber Bragg grating inscription in indium fluoride fiber using a UV/Vis femtosecond laser and two-beam interferometry, Opt. Lett. 46 (2021) 1816, https://doi.org/10.1364/OL.420264.
[140] R. Liu, Z. Luo, L. Wu, J. Ran, Y. Wang, C. Lv, S. Qin, Z. Bai, Y. Wang, S. Liu, C. Liao, Y. Wang, Efficient inscription of high quality FBGs on ZBLAN fiber with a femtosecond laser, J. Light. Technol. 43 (2025) 4429–4434, https://doi.org/10.1109/JLT.2025.3531007.
[141] K. Grebnev, A. Sultanov, G. Oelsner, I. Chiamenti, M. Chernysheva, Thermal properties of fluoride fiber Bragg gratings at high to cryogenic temperatures, Opt. Lett. 49 (2024) 6589, https://doi.org/10.1364/OL.545902.
[142] M. Heck, S. Nolte, A. Tünnermann, R. Vallée, M. Bernier, Femtosecond-written long-period gratings in fluoride fibers, Opt. Lett. 43 (2018) 1994, https://doi.org/10.1364/OL.43.001994.
[143] L. She, Q. Qi, P. Zhang, S. Dai, Y. Jiang, W. Sun, S. Jia, S. Wang, G. Brambilla, P. Wang, Mid-infrared fluoroindate glass long-period fiber grating by femtosecond laser inscription, Infrared Phys. Technol. 116 (2021) 103808, https://doi.org/10.1016/j.infrared.2021.103808.
[144] A. Theodosiou, Y. Baravets, K.V. Grebnev, M. Chernysheva, P. Honzatko, P. Peterka, Fluoride Long Period Grating developed using filament fusion splicer, in: Adv. Photonics Congr, Optica Publishing Group, Québec City, 2024, https://doi.org/10.1364/BGPP.2024.JTu1A.10, 2024: p. JTu1A.10.
[145] F. Anelli, A. Annunziato, A.M. Loconsole, P.L. Pays Du Teilleul, S. Cozic, F. Prudenzano, LPG in fluoride optical fiber via micro-tapering technique: mid-IR mode coupling, J. Light. Technol. 43 (2025) 2803–2810, https://doi.org/10.1109/JLT.2024.3496501.
[146] L.J. Arevalo-Bautista, R. Selvas-Aguilar, J.M. Sierra-Hernandez, E. Gallegos-Arellano, M.A. Rico-Mendez, P.J. Fernandez De Cordoba-Castella, D. Toral-Acosta, Displaced thinned single-mode fiber Mach-Zehnder interferometer tested for temperature and curvature applications, Results Opt 17 (2024) 100744, https://doi.org/10.1016/j.rio.2024.100744.
[147] F. Anelli, S. Venck, S. Cozic, F. Prudenzano, S-tapered fluoride optical fiber for refractive index sensing in the mid-infrared, J. Light. Technol. (2025) 1–7, https://doi.org/10.1109/JLT.2025.3552855.
[148] K. Goya, Y. Koyama, Y. Nishijima, S. Tokita, R. Yasuhara, H. Uehara, A fluoride fiber optics in-line sensor for mid-IR spectroscopy based on a side-polished structure, Sens. Actuators B Chem. 351 (2022) 130904, https://doi.org/10.1016/j.snb.2021.130904.